VCE
VIBRANT CLEAN ENERGY

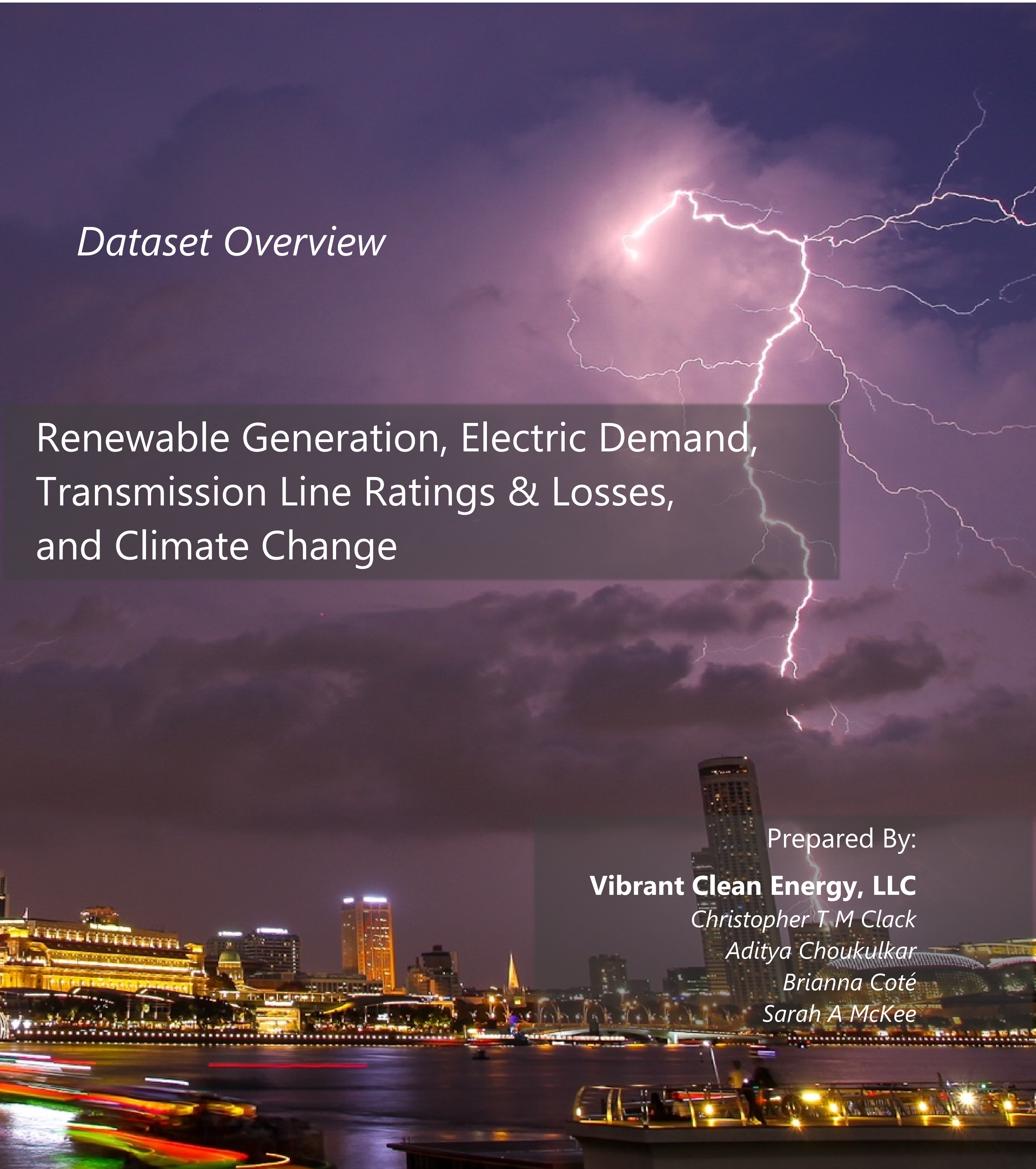

Dataset Overview

Renewable Generation, Electric Demand, Transmission Line Ratings & Losses, and Climate Change

Prepared By:

Vibrant Clean Energy, LLC
Christopher T M Clack
Aditya Choukulkar
Brianna Coté
Sarah A McKee

Table of Contents

1.1 Renewable Generation Dataset - 3 -
1.1.1 Wind power dataset method - 4 -
1.1.2 Solar power dataset method - 13 -
1.1.3 Temperature power dataset method - 24 -

1.2 Electric Demand Dataset - 25 -
1.2.1 Traditional demand profiles - 25 -
1.2.2 Space heating demand profiles - 27 -
1.2.3 Water heating demand profiles - 28 -
1.2.4 Space heating flexibility - 29 -
1.2.5 Transportation demand profiles - 30 -

1.3 Removing Space, Water Heating and Transport from Historical Electricity Use - 33 -

1.4 Transmission Line Rating & Electric Losses Dataset - 35 -

1.5 Climate Change Dataset - 40 -
1.5.1 Changes to wind energy production potential - 41 -
1.5.2 Changes to solar PV energy production potential - 43 -
1.5.3 Changes to thermal generator heat rates & water - 45 -
1.5.4 Changes to line ratings & electric losses - 46 -
1.5.5 Changes to space heating demand - 48 -
1.5.6 Changes to water heating demand - 50 -
1.5.7 Changes to conventional & cooling demand - 51 -
1.5.8 Changes to transportation demand - 53 -

1.6 Bibliography - 55 -

1.1 Renewable Generation Dataset

Weather is an integral component to modeling generation from variable renewable energy sources (such as wind and solar), the efficiency of conventional generators, the transmission ampacity and electric losses, and the electric demand profiles (specifically traditional demands, electric space heating, electric water heating and electric vehicle charging).

The raw weather data is obtained from the National Oceanic and Atmospheric Administration (NOAA) High Resolution Rapid Refresh (HRRR) weather forecast model, which is a specially configured version of Advanced Research WRF (ARW) model. The HRRR is run every hour over a 3-km horizontal resolution that covers the continental United States as well as portions of Canada and Mexico. Since its inception, HRRR has undergone rapid and continuous improvement to its physical parameterization schemes, many of which have specifically targeted improved forecasts for the renewable energy sector. Through collaborative research efforts between the Department of Energy (DOE) and NOAA, projects such as the Solar Forecast Improvement Project [1], the Wind Forecast Improvement Projects I and II [2], [3] were conducted to improve forecasts of meteorological quantities important for wind and solar energy.

1.1.1 Wind power dataset method

The amount of wind power captured by a wind turbine is proportional to the cube of the wind speed directed into the wind turbine, parallel to the rotor. As wind turbines have grown taller and the rotor swept area has increased, different portions of the wind turbine rotor are exposed to (significantly) different conditions of wind speed, temperature, air density and precipitation. Therefore, it is critical to capture these impacts of varying meteorological conditions with height on wind power production in modeling. VCE® incorporates these profiles of meteorological conditions using the rotor equivalent formulations [4], [5]. The VCE® wind power model is described in the present section.

The VCE® wind power dataset is created using the HRRR weather forecast outputs. VCE® stores the HRRR outputs for forecast hours 0 (also known as initialization), 2, 6, and 12. The forecast hour 2 output has been found to be the most accurate, and thus is used for the wind power calculations[1]. The following variables are used to create the VCE® wind power dataset:

- *Horizontal components of wind (u, v)*
- *Pressure (P)*
- *Temperature (T)*
- *Specific humidity (spH)*
- *Geopotential height (GPT)*
- *Cloud-water mixing ratio (cwr)*
- *Rain-water mixing ratio (rwr)*
- *Wind gust at lowest level (WG)*

The HRRR variables are output on three different vertical coordinates: Pressure coordinates, Terrain following sigma coordinates, a Hybrid vertical coordinates. The hybrid vertical coordinate mitigates the small-scale noise found near steep terrain, while having better vertical resolution than the pressure coordinates. Figure 1.1 shows an example horizontal transect through complex terrain. It can be seen that the vertical velocity fields are much more realistic in magnitude and less noisy in the hybrid coordinate.

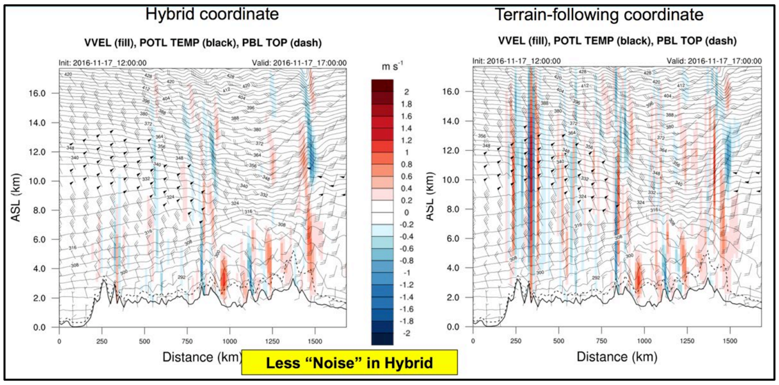

Figure 1.1: Reduction in noise in the hybrid coordinate (left) compared to the terrain following coordinate (right).

The HRRR model outputs do not include density and needs to be calculated. Density is calculated using a modified formulation of the ideal gas law

---

[1] During periods where forecast hour 2 is missing, the corresponding forecast hour 0 is used and for periods where forecast hour 0 is also missing, the corresponding forecast hour 6 is utilized.

$$\rho = \frac{P_o^{0.2854} P^{(1-0.2854)}}{RT_v} \tag{1}$$

where R is the specific gas constant (287.058 $\mathrm{Jkg^{-1}K^{-1}}$ for dry air) and T_v is the virtual potential temperature, which is calculated using the formula

$$T_v = \frac{T}{\left({}^{P}/_{P_o}\right)^{\kappa}} \left(1 + 0.61spH - \ (cwr + rwr)\right) \tag{2}$$

Here P_o is the standard pressure which is 10^5 Pa and κ is the Poisson constant given by

$$\kappa = 0.2854 * (1 - 0.24 * spH) \tag{3}$$

The modified formulation is utilized to account for the buoyancy effects for the change in temperature and pressure with height above the ground. The buoyancy effect is captured by the virtual potential temperature calculated in Eq (2). The horizontal wind speed components (*u*,*v*), density, temperature and cloud-water mixing ratio are interpolated for heights 20 m above the ground to 300 m above the ground with 15 m vertical resolution. The HRRR wind gust outputs are used to compute a gust factor expressed as a fraction of the mean wind speed.

1.1.1.1 Rotor equivalent calculations

Wind turbine power generation potential is derived as the kinetic energy flux through the wind turbine rotor layer. This general relationship is shown in Equation (4)

$$P_w = \frac{1}{2} C_p \rho A U^3 \tag{4}$$

where C_p is the coefficient of power (ratio of actual power generated to available power in the wind), ρ is the air density, A is area of the wind turbine rotor and U is the horizontal wind velocity component along the horizontal axis of the wind turbine rotor. The vertical component of the velocity does not contribute appreciably to wind power production as modern wind turbines use aerodynamic lift for propulsion. In addition, any drag-component due to vertical velocity is assumed to cancel out over the rotor swept area. Equation (4) is valid as long as the density and velocity do not change within the rotor swept area of the wind turbine. However, modern wind turbine rotors can span vertical extents of 100 m or more and the variables that impact wind power production can change significantly within this vertical extent (Figure 1.2).

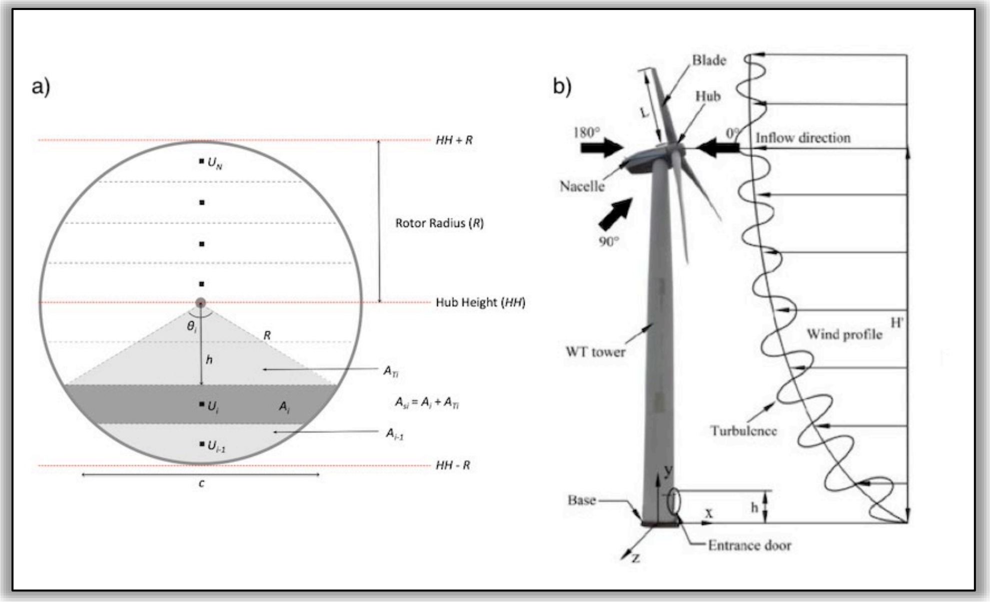

Figure 1.2: Schematic showing how the wind profile can change within the rotor layer and how the wind turbine rotor is divided to calculate the rotor equivalent variables.

The rotor equivalent formulation provides a more accurate estimate of wind power production by taking into account the vertical profile of the variables affecting wind power production. At its core, the rotor equivalent formulation allows calculation of the area weighted mean of the various meteorological variables across the wind turbine rotor. The rotor area is divided into sections with respect to height equal to the vertical resolution of the dataset (15m). Each of the variable values at a given height is area weighted by the portion of the wind turbine rotor it represents (equal to the vertical resolution) in order to estimate the equivalent effect of the vertical profile of that variable. Equations (5) and (6) show how the speed and density in Equation (4) can be replaced by their rotor equivalent counterparts.

$$U_{eq} = \frac{1}{A} \sum_i \frac{u_i u_H + v_i v_H}{U_H} A_i \tag{5}$$

$$\rho_{eq} = \frac{1}{A}\sum_{i} \rho_i A_i \tag{6}$$

In Equation (5), the effect of turbulence is neglected. The effect of turbulence can be included in the power calculations using Equation (7), as derived in [5]:

$$U_{eqT} = \frac{1}{A}\sum_{i} \frac{(u_i + u_i')(u_H + u_H') + (v_i + v_i')(v_H + v_H')}{[(u_H + u_H')^2 + (v_H + v_H')^2]^{1/2}} A_i \tag{7}$$

where $(.)'$ denotes tendency of that variable in a given time period (5-min in our case). Equation (7) shows that the effect of turbulence results in additional wind power being generated, which makes sense analytically as turbulence represents additional energy in the wind. However, actual wind turbine response to turbulence results in additional power generated at the lower end of the power curve (due to the additional energy). It also results in under-performance at the higher end of the power curve due to the positive velocity fluctuations being damped by the wind turbine control [6]. The effect of turbulence on power production due to wind turbine control can only be modelled through a full mechanical modeling of the wind turbine as is done by the National Renewable Energy Laboratory (NREL) FAST software. In our analysis, this effect of turbulence is neglected as it is found to be much smaller compared to the effect of wind speed and direction shear [5].

The rotor equivalent formulation takes into account the change in density with respect to height as well as wind speed and direction shear on wind turbine power potential calculations. The rotor equivalent formulation is also applied to the temperature and moisture information as shown in Equations (8) and (9). The rotor equivalent temperature and moisture information is used to determine icing possibility within the wind turbine rotor.

$$T_{eq} = \frac{1}{A}\sum_{i} T_i A_i \tag{8}$$

$$cwr_{eq} = \frac{1}{A}\sum_{i} cwr_i A_i \tag{9}$$

The rotor equivalent quantities are then linearly interpolated to 5-min intervals for each of the HRRR grid cells. The linear interpolation also covers any possible periods of data outages. These 5-min rotor equivalent quantities are used in the power calculations. In order to calculate actual power generation from the theoretical available power in the wind a C_p curve is used. A C_p curve is the ratio of the actual electrical power generated for a given wind speed to the theoretical available power in the wind given by Equation (10)

$$C_p = \frac{P(u)}{P_{wind}(u)}. \tag{10}$$

As the wind moves passed the wind turbine blades, it transfers momentum to the turbine blades and produce electricity. This transfer of momentum from energy extraction results in the control volume of the wind passing through the turbine to expand downstream of the rotor to preserve continuity. Based on this, [7] calculated the theoretical maximum energy that can be extracted by a wind turbine. This theoretical maximum, called the Betz limit, is equal to 59.3% and is the maximum value a C_p can take.

The C_p curve varies for different types of wind turbines. The International Electrotechnical Commission (IEC) described four classes for wind turbines: Classes I, II, III and offshore. The shape of the C_p curve is defined not only by the physical limits on converting wind power to electricity, but also the control strategies employed by the wind turbine. For all onshore locations, the IEC-III curve is used and the offshore curve is used for all offshore locations.

To accurately calculate wind power generation, the following two components are important and depend on how the C_p curve is used:

- The impact of turbulence on power generation;
- Wind turbine response to changes in air density.

1.1.1.2 Effect of turbulence

As described earlier, turbulence has a complicated impact on the wind power generation. At wind speeds closer to the cut-in speed, the presence of turbulence increases power generated from the turbine, while at wind speeds closer to the rated power, turbulence reduces the power output from a wind turbine [6]. The reason for this behavior is that near cut-in speed, the positive fluctuations due to turbulence are allowed to generate excess power, while the negative fluctuations do not have any effect as the turbine is not generating any power in that case. Near the rated speed, the positive fluctuations due to turbulence get damped out by the wind turbine control, while the negative fluctuations reduce power output, and hence the net effect is a reduction in power output from the turbine.

Modelling this effect analytically is difficult as seen from Equation (7), where presence of turbulence always results in increased power production. Therefore, instead of trying to model this effect analytically, it was decided to utilize the characteristics of the C_p curve to simulate the wind turbine control response. To do this, the HRRR model wind speed output needs to be perturbed in a manner that actual atmospheric turbulence would, as shown in Equation (11), known as the Reynold's decomposition.

$$U(t) = \overline{U}(t) + u'(t) \tag{11}$$

where, $U(t)$ is the wind speed including effect of turbulence at given timestep, $\overline{U}(t)$ is the mean wind speed at a given timestep from the HRRR, and $u'(t)$ is the random turbulence perturbation at that timestep.

The perturbations that need to be added to the HRRR model wind speed are estimated using the wind gust HRRR model output. The HRRR model estimate of wind gust represents a sudden, brief increase in peak wind speed (lasting less than 20 seconds) expected at a given timestep. An estimate of the standard deviation of turbulence from this peak value is needed. Assuming that the turbulence distribution is symmetric (skewness of zero), which is reasonable for horizontal velocity turbulence, and that it follows a standard normal distribution, the standard deviation can be estimated using Equation (12):

$$\sigma_U = \frac{\left(U_{gust} - U_{eq}\right)}{4} \tag{12}$$

where, U_{gust} is the model outputted wind gust at a given timestep, U_{eq} is rotor equivalent wind speed from Equation (5), and σ_U is the standard deviation of wind speed due to turbulence.

The reasoning used in Equation (12) to calculate standard deviation is based on the following. Since the gust is the peak wind speed observed, it is assumed to be a value in the 99.9936th percentile which is four standard deviations from the mean. The standard deviation of wind speed due to turbulence calculated using Equation (12) is now used to calculate the random perturbation to the rotor equivalent wind speed at a given timestep using Equation (13):

$$U_{eqT}(t) = U_{eq} + rand(0, \sigma_U) \tag{13}$$

where, U_{eqT} is the rotor equivalent wind speed including the effect of turbulence. The rest of the calculations proceed as described earlier.

1.1.1.3 Wind turbine response to density fluctuations

Modern wind turbines have control responses to maximize wind generation in presence of changing air densities. This control response is usually active close to the rated wind speed, but can also extend to region 2 of the power curve. Figure 1.3 shows the turbine response in terms of the observed C_p values in response to changes in air density.

As seen in Figure 1.3 the C_p value is a function of both wind speed and density (top panel) and the changes in C_p values compared with the C_p value at standard density are highly non-linear (bottom panel). However, the change in C_p with respect to density at a given wind speed is linear. The slope and intercept of this linear behavior changes at every wind speed. Therefore, a model was constructed to predict the slope and intercept of the change in C_p at a given wind speed. This model allows predict of a "correction" to the C_p at standard density and given wind speed, which will produce the correct C_p value at that wind speed and density.

Figure 1.3 shows the comparison of the described model predicted C_p values against the actual manufacturer supplied C_p values. It is seen that the model is able to predict the changes to the C_p values at various densities and wind speeds accurately. The comparison of the C_p values at various densities to the C_p values at the standard density (1.225 kg/m^3) show that there can be differences of up 50% of the C_p value at a given wind speed. Hence it is very important to quantify the impact of density on the C_p values.

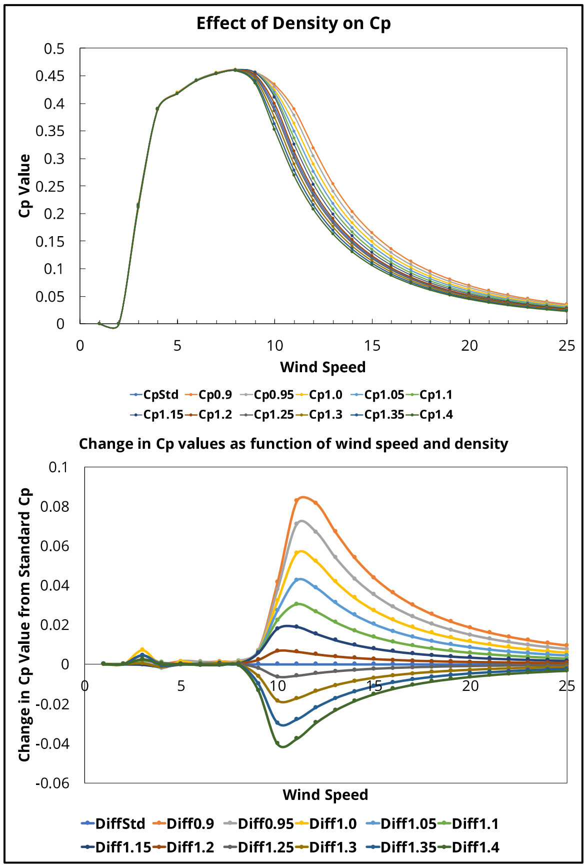

Figure 1.3: Impact of density on C_p values for a 2.3 MW Siemens wind turbine.

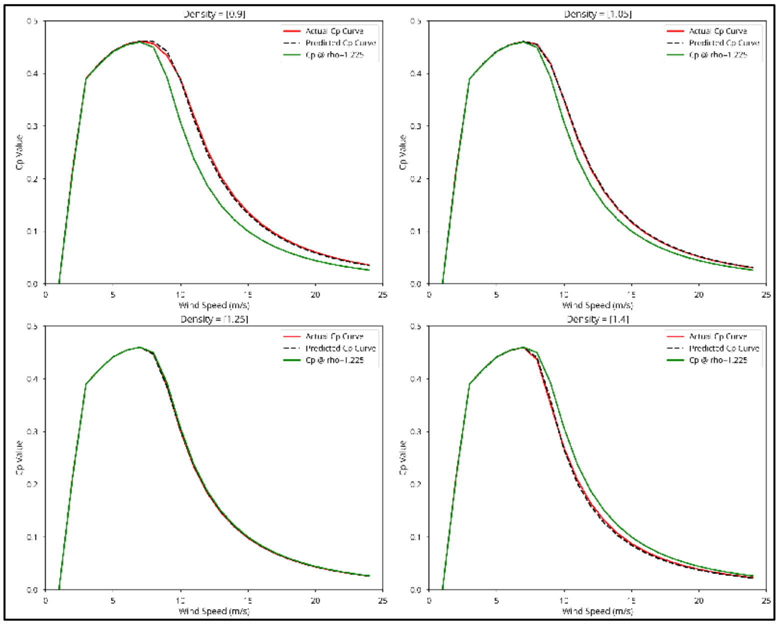

Figure 1.4-A: Comparison of model predicted C_p (black dashed line) values to the actual turbine C_p values (red solid line). The standard C_p value at density of 1.225 kg/m^3 is shown in solid green line.

Starting in 2019, VCE® has begun to pull higher model heights up to 360 meters. This is increased from 300 meters previously and is used to provide rotor equivalent wind speed for hub heights up to 200 meters. Before 2019, hub heights are only available up to 160 meters. In addition, VCE® now incorporates the NREL 15 MW reference turbine for offshore sites greater than a 140-meter hub height. Offshore technology has experienced vast improvements over the recent years. Integrating this improved capability into WIS:dom® allows for the development potential of offshore in the model to match these technology advancements. Figure 1.4-B shows the new offshore power curve is more aggressive and produces more power from a lower wind speed across all wind speed bins plotted.

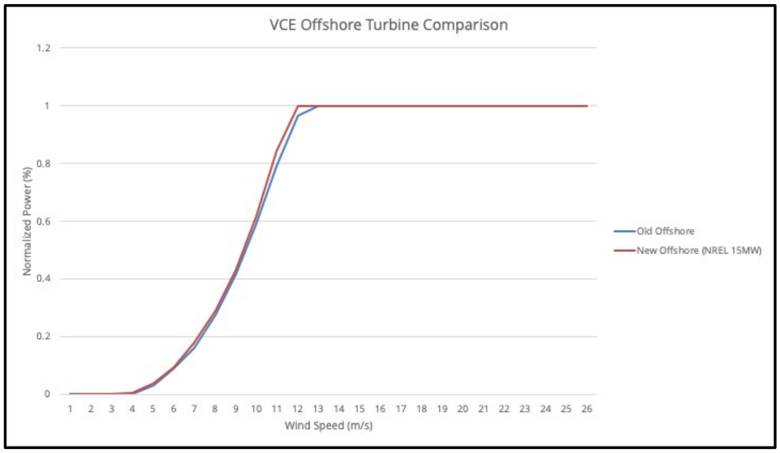

Figure 1.4-B: Comparison of the previous VCE offshore power to the new NREL 15MW reference power curve now used when deriving the wind generation dataset. This is utilized for offshore sites where hubs heights are greater than 140-meters.

The WIS:dom® model takes into account time periods where generation may not be possible due to extreme weather conditions. Normal operational temperatures for wind turbines are set to be between -25°C and 45°C. In addition, the potential for icing is also calculated. Icing is considered possible when temperatures are below -15°C and cloud-water mixing ratio is greater than zero. The periods with potential for icing or temperatures outside of normal operating conditions are set to zero power output. It is important to identify periods such as the above where generation will be limited or zero as these are usually correlated with periods of high energy demand. WIS:dom® then has to ensure that the demand during these periods will be met in some other way.

The above power calculations are performed for each 3-km HRRR grid cell (~1.9 million grid cells) for all the years required to run WIS:dom®. The WIS:dom® model is run on the same grid as the HRRR, however, only a subset of the HRRR cells are made available for wind plant development. The potential for wind development in MW for each HRRR cell is made available to WIS:dom®, which is used in determining whether wind generation gets built or not. The available wind capacity potential provided to WIS:dom® is shown in Figure 1.5(d). When choosing to build wind generation, WIS:dom® can choose the most optimal hub-height wind turbine to build. As seen from Figure 1.5 (a) and 1.5(c), higher hub-heights give higher wind power capacity factors. However, there are additional costs associated with building taller towers and wind turbines capable to withstanding higher wind loading. WIS:dom® takes these costs into account and determines the optimal hub-height at a given location. The optimal height is determined by evaluating whether the increased cost due to the higher tower height is offset by increased revenue or demand met from additional power generation at the higher hub-height. In this analysis it is assumed that the same turbine rotor is installed on taller towers. An important impact of this assumption is that as the hub-heights increases, the wind power capacity factors also increase due to the higher average wind speeds at increased heights above the ground. However, beyond a certain hub-height, wind power capacity factors start to decrease. This decrease in power capacity factors is due to increased wind speeds at higher hub-heights, the wind turbines are in the cut-off portion of the power curve more often. Therefore, to take full advantage of the increased wind resource at higher heights will require a redesign of the turbine rotor to operate in the higher wind speed regime.

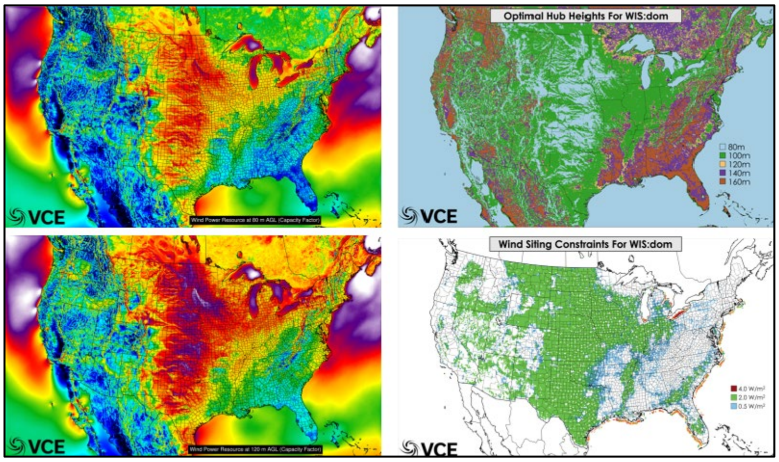

Figure 1.5: The wind power dataset. Mean wind power capacity factor at for 80-m hub-height using data from year 2014 (top left), optimal hub-height for the CONUS (top right), mean wind power capacity factor for 120 m hub-height using data from year 2014 (bottom left), and wind plant siting constraints for the CONUS (bottom right).

1.1.2 Solar power dataset method

Calculation of the solar PV power generation requires accurate forecasts of Global Horizontal Irradiance (GHI), Direct Normal Irradiance (DNI) and Diffuse Horizontal Irradiance (DHI). These variables are then input into a PV cell power modeling algorithm. The components of the solar irradiances are related to each other by:

$$GHI = DNI*\cos(sza) + DHI \tag{14}$$

where *sza* is the solar zenith angle.

Numerical weather prediction models did not output forecasts of DNI and DHI until 2016. In addition, forecasts of DNI and DHI produced by the HRRR after 2016 have significant biases mainly due to improper representation of clouds. To obtain forecasts of DHI and DNI from HRRR model outputs for years before 2016 and correct for model biases for years after 2016, VCE® employs a linear multiple multivariate regression technique developed by [8]. The variables used to create the solar power data are the following:

- From the HRRR
  - ✓ *Downwelling shortwave (SW),*
  - ✓ *Downwelling longwave (LW),*
  - ✓ *10-m wind speed (Wind10m),*
  - ✓ *2-m temperature (T2m),*
  - ✓ *Direct normal irradiance (DNI) – 2016 onwards,*
  - ✓ *Diffuse horizontal irradiance (DHI) – 2016 onwards,*
- From GOES-east and GOES-west (for datasets before 2016 only)
  - ✓ *Visible band,*
  - ✓ *4μm band,*
  - ✓ *11μm band,*
  - ✓ *13μm band,*
  - ✓ *Water-vapor band,*
- Calculated
  - ✓ *Direct normal irradiance at the top of the atmosphere* (DNI_0)*,*
  - ✓ *Solar zenith angle (sza),*
  - ✓ *Solar azimuth angle (azm),*
  - ✓ *Hour-angle (hrang),*
  - ✓ *Declination angle (dec).*

The satellite observations are not included starting in 2016, as these observations are already assimilated into the HRRR during data assimilation. To perform the regression, we get observations of GHI, DNI and DHI from fifteen ground-based radiation measurement sites (SURFRAD and SOLRAD) operated by the NOAA. The above variables are chosen as they are most likely to impact the amount of solar irradiance reaching the Earth's surface and its attenuation along the way. A significant portion of the effort in creating the solar power dataset is spent on getting the data ready for regression. First, the required HRRR variables are extracted from the HRRR output files at 1-hour resolution. These HRRR variables are then linearly interpolated to 5-min intervals. For data gaps of longer than 1-hour, persistence is assumed and they are filled in with data from the same hour on the previously available day. Linear interpolation is carried out only sub-hourly.

Satellite measurements from GOES-east and GOES-west are used, which allows a stereoscopic observation of the cloud field. Each of the GOES satellite observations cover the full CONUS with observations available at 15-min time interval. The GOES satellites make measurements in 5-channels listed above. The measurements are in bit count, which are converted to temperature (in Kelvin) using the formula [8]:

$$T = \frac{1}{2}(660 - B), \quad 0 \leq B \leq 176 \quad and \\ T = 418 - B, \;\; 176 < B \leq 255 \qquad (15)$$

The spatial resolution of the satellite data is 1-km for the visible channel and 4.km for the remaining channels. Since the HRRR has a spatial resolution of 3-km, the satellite data are spatially interpolated on to the HRRR grid. This spatially interpolated satellite data is then linearly interpolated in time to 5-min intervals to match the interpolated HRRR output.

In addition to the variables obtained from the HRRR and satellite measurements, five additional variables are calculated. The calculation of solar irradiance at the top of the atmosphere needs to take into account the eccentricity of Earth's orbit. The average DNI_0 at the top of the atmosphere is 1360.8 W m^{-2} and is denoted by I_o. The equation for the actual irradiance hitting the top of the atmosphere is given by

$$DNI_0 = I_o \left(\frac{R_{avg}}{R}\right)^2 \qquad (16)$$

where R_{avg} is the average Earth-Sun distance and R is the instantaneous Earth-Sun distance. The ratio of R_{avg} to R is given by the Fourier expansion in Equation (16) which is accurate to 0.0001 [9]

$$\left(\frac{R_{avg}}{R}\right)^2 \approx 1.000110 + 0.034221\cos(\delta) + 0.00128\sin(\delta) + 0.000719\cos(2\delta) + 0.000077\sin(2\delta) \qquad (17)$$

where, the day angle $\delta = {}^{2\pi d}/_{365.242}$ radians and d is the day of the year.

The declination angle is also given as a Fourier expansion in Equation (18) which accurate to 0.0006 radians [9]

$$dec = 0.006918 - 0.399912\cos(\delta) + 0.070257\sin(\delta) - 0.006758\cos(2\delta) + 0.000907\sin(2\delta) \\ - 0.002697\cos(3\delta) + 0.00148\sin(3\delta) \qquad (18)$$

The hour angle, given by equation (19) is defined as the number of degrees the Sun moves across the sky compared to local Solar noon. The hour angle is zero at local Solar noon, positive in the afternoon and negative in the morning

$$hrang = 15 * (LST - 12), \qquad (19)$$

where LST is the local solar time given by

$$LST = LT + \frac{TC}{60} \qquad (20)$$

where LT is the local time and TC is the time correction factor that accounts for the variation in the local Solar time due to the range of longitudes within the same time zone, eccentricity of the Earth's orbit and

Earth's axial tilt (to calculate the last two, the equation of time given by Equation (23) is used). The time correction factor (*TC*) is calculated as

$$TC = 4 * (lon - LSTM) + EoT \tag{21}$$

where, *LSTM* is the local standard time meridian is the reference meridian used for a particular time zone and is calculated using the equation

$$LSTM = 15 * (LT - UTC) \tag{22}$$

and *EoT* is the equation of time, which is an empirically derived relationship that corrects for the eccentricity of the Earth's orbit and the Earth's axial tilt. The *EoT*, in radians, is given by a Fourier expansion that is accurate to 0.0025 radians or 35 seconds [9]

$$EoT = 0.000075 + 0.001868\cos(\delta) - 0.032077\sin(\delta) - 0.014615\cos(2\delta) - 0.040849\sin(2\delta). \tag{23}$$

Now the Solar zenith angle can be calculated using Equation (24)

$$\cos(sza) = \sin(lat)\sin(dec) + \cos(lat)\cos(dec)\cos(hrang) \tag{24}$$

where, the latitude (*lat*), declination angle (*dec*) and hour angle (*hrang*) are in radians.

Once all the quantities required for the regression are collected, the regression can be performed. The regression is performed separately for the GHI and DNI for computational efficiency and DHI is calculated using Equation (14) once the GHI and DNI are known. The regression is represented mathematically as [8]

$$Y_{n\times p} = X_{n\times(r+1)}\beta_{(r+1)\times p} + \varepsilon_{n\times p} \tag{25}$$

where, $Y_{n\times p}$ are the endogenous variables (here the ground-based measurements of GHI, DNI and DHI), $X_{n\times(r+1)}$ are the exogenous variables (here the variables from the NWP model, satellite measurements and calculated variables), $\beta_{(r+1)\times p}$ are the regression coefficients and $\varepsilon_{n\times p}$ are the measurement errors in the ground-based observations.

The ground-based observations of the irradiance components measured by the SURFRAD and SOLRAD sites are available at 1-min time resolution. These measurements are averaged to 5-min resolution, which reduces measurement noise and helps reduce the discrepancy between a point measurement from the SOLRAD/SURFRAD sites and the grid-cell average from the HRRR model. The errors in the SURFRAD/SOLRAD observations are modelled as

$$\varepsilon = 5 + 0.02 * (1 - \cos(sza)) + 0.01 * T2m + 0.005 * GHI. \tag{26}$$

The SURFRAD/SOLRAD measurements are known to have error bars of ±5 W m^{-2} under ideal conditions. These errors get larger depending on various factors such as total irradiance, ambient temperature and solar zenith angle. The regression is performed using the advanced statistics package from IDL and analysis of variance (ANOVA) techniques are used to determine performance of the regression. The regression coefficients that give the best performance are applied to the HRRR data to get irradiance estimates over the whole contiguous United States. Once the irradiance components are calculated, the power production from a photovoltaic panel can be estimated.

1.1.2.1 Estimating power from solar photovoltaics

A photovoltaic (PV) cell converts solar radiation incident on its surface to electrical power. A PV cells utilizes both the direct (DNI) and diffuse (DHI) radiation to produce current and a voltage, which determine the power generated by the cell as shown in Figure 1.6 and is defined by Equation (27):

$$P_s = V * I. \tag{27}$$

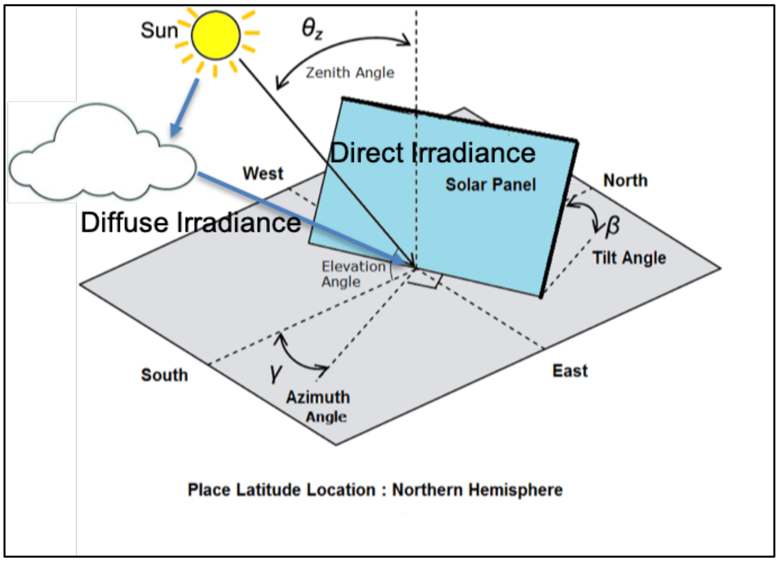

Figure 1.6: Schematic showing the direct and diffuse irradiance on a PV panel with respect to its tilt and azimuth orientation.

The power performance of a PV cell is a complex function of several environmental factors (such as ambient temperature, wind speed, incident irradiation) as well as the PV cell characteristics. These environmental factors interact non-linearly and make estimating the power output from a PV cell difficult. The power performance model used by VCE® is an empirically derived model developed by Sandia National Laboratory and described in [10]. To calculate the voltage and current induced in the PV cells, equations (11) to (20) from [10] are used. These equations attempt to model the non-linear response of a PV cell as an interaction of several factors each having well defined, experimentally derived relationships with the independent variables affecting PV cell performance.

To calculate the power produced from a PV cells requires being able to model the shape of the I-V curve of the PV panel accurately. The I-V curve of a PV cell shifts depending on the amount of incident radiation on the panel and ambient temperature. In order to replicate these effects accurately King et al. [10] model the voltage and current response separately using 3,300 measurements made over a range of clear and cloudy conditions, wide range of solar irradiance and module temperatures. The measured voltage values are first translated to a common temperature of 50ºC to remove effects of temperature. The translated measurements of voltage and associated irradiance are regressed using Equations (28) and (29) to find values of *n*, c_2 and c_3:

$$V_{oc} = V_{oco} + N_s\delta(T_c).\ln(E_e) + \beta_{Voc}E_e(T_c - T_o) \tag{28}$$

$$V_{mp} = V_{mp0} - c_2N_s\delta T_c\ln(E_e) - c_3N_s(\delta T_c\ln(E_e))^2 - \beta_{vmp}E_e(T_c - T_o) \tag{29}$$

where V_{oc} is the open-circuit voltage, V_{oco} is the open-circuit voltage constant, V_{mp} is the voltage at maximum power, V_{mp0} is the constant for voltage in I-V curve, $\delta(T_c) = n\,k\,(T_c + 273.15)/q$ is the thermal voltage per cell at temperature T_c, n, c_2, c_3 are constants for voltage formula, q is the elementary charge (1.60218e-19 coulomb), k is the Boltzmann's constant (1.38066e-23 J K^{-1}), N_s number of cells in series in a module's cell-string, T_o reference cell temperature, $T_c = GHI * e^{a+b*WS} + T_{2m}$ is the cell temperature inside the module, WS is the wind speed, T_{2m} is the 2-m temperature, and a, b are constants.

In a similar way, to determine the dependence of module current on incident irradiation, the current values are translated to a common temperature and regression coefficients, C_o, C_1, C_4, C_5, C_6, C_7, are determined using Equations (30), (31) and (32):

$$I_{mp} = I_{mpo}\{C_0 E_e + C_1 E_e^2\}\{1 + \alpha_{Imp}(T_c - T_o)\} \tag{30}$$

$$I_x = I_{xo}\{C_4 E_e + C_5 E_e^2\}\{1 + \alpha_{Isc}(T_c - T_o)\} \tag{31}$$

$$I_{xx} = I_{xxo}\{C_6 E_e + C_7 E_e^2\}\{1 + \alpha_{Imp}(T_c - T_o)\} \tag{32}$$

where, I_{mp} is the current at maximum power, I_{mp0} is the constant for current in I-V curve, I_x is the current at module V = 0.5 V_{oc}, I_{xx} is the current at module V = 0.5 $(V_{oc} + V_{mp})$, I_{x0} is the constant for current in I-V curve, I_{xx0} is the constant for current in I-V curve, α_{Imp} is the normalized temperature coefficient for I_{mp}, and α_{Isc} is the normalized temperature coefficient for I_{sc}, the short-circuit current.

In the above equations, E_e is the effective irradiance to which the PV cells in the module respond to and is given by

$$E_e = f_1 * SF * \left[\frac{E_b f_2 + f_d * DHI}{E_o}\right] \tag{33}$$

where, $E_b = DNI * \cos(AOI)$, which is the beam component of the solar irradiance incident on module surface, E_o is the reference solar irradiance (1000 W/m^2), f_1 is the relation between solar spectral variation and short circuit current given by $f_1 = a_0 + a_1 AM_a + a_2 AM_a^2 + a_3 AM_a^3 + a_4 AM_a^4$, where a_0, a_1, a_2, a_3, a_4 are constants and AM_a is the absolute air-mass (dimensionless), SF is the soiling factor, f_2 is the relation between optical influences and solar angle-of-incidence, $f_2 = b_0 + b_1 * AOI + b_2 * AOI^2 + b_3 * AOI^3 + b_4 * AOI^4$, where b_0, b_1, b_2, b_3, b_4 are constants, $AOI = \cos\beta\cos\theta_z - \sin\beta\sin\theta_z\cos\gamma$ is the angle of incidence, where β is tilt angle of the panel with respect to the ground, θ_z is solar zenith angle, γ is the azimuth angle with respect to the north-south, and f_d is the relative response to diffuse versus beam irradiance.

The empirical functions $f_1(AM_a)$ and $f_2(AM_a)$ quantify the effect of solar spectral variation and optical influences on short-circuit current. These functions are determined from laboratory testing and account for systematic effects that occur during clear sky periods. Absolute airmass provides a relative measure of the path length solar radiation has to travel at a given solar zenith angle compared to a solar position of directly overhead.

The performance of a PV panel also depends on the module temperature as seen in Equations (28)-(32). The thermal response of a PV cell can be modelled as

$$T_c = GHI * e^{a+b*WS} + T_{2m}. \tag{34}$$

The simple model for expected module temperature given by Equation (31) has been shown to have accuracy of ±5°C, which results in uncertainty in power output of less than 3%.

The constants in the power generation model are obtained from [11] and the NREL System Advisory Model (SAM) [12]. It is assumed that the individual panels are placed far enough apart so as not to create any shadowing effects. The above formulae are used to calculate solar power production for the following technologies:

- *Fixed PV panel for various tilt angles (0°, 15°, 30°, 45°, latitude tilt),*
- *One-axis tracking at latitude tilt,*
- *Two-axis tracking.*

Finally, the calculated power output is de-rated based on expected losses from wiring and soiling (4.5% loss), AC/DC conversion (3.3% loss) and presence of snow on the panels (assume no production if snow is present – for fixed panels at 0° and 15° elevation). WIS:dom® can update the magnitude of these losses to account for improved technology in the future or panel performance degradation with age.

The technologies for utility scale PV range from simplest and least cost (Fixed panels with 0-degree tilt) to most complex and highest cost (dual-axis panels). The fixed panels at 0-degree tilt will result in the lowest power capacity factors while the dual-axis panels will result in the highest as they track the sun across the sky to ensure maximum possible power production [see Figure 1.7-A (top-left and bottom-left panels, respectively)]. WIS:dom®-P can determine using the weather data if the added complexity of the PV technologies is worth the additional cost in terms of increased power production. As seen from Figure 1.7-A (top-right panel), Fixed panels at various elevation angles (with respect to the latitude of the geographic location) are the optimal choice for most of the CONUS with only the northern-most part of the country justified in using either single or dual axis tracking.

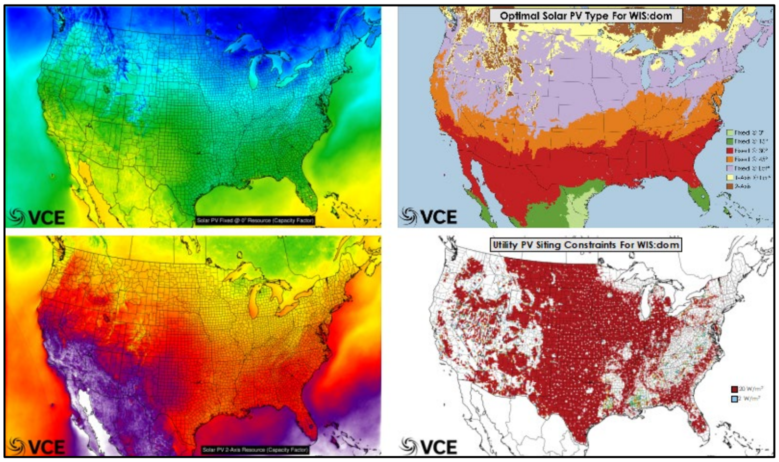

Figure 1.7-A. The solar power dataset. Mean solar PV capacity factor for fixed panel at 0° elevation for year 2014 (top left), mean solar PV capacity factor for a two-axis tracking PV panel for year 2014 (bottom left), optimal PV panel type for the CONUS (top right), and utility PV siting constraints for the CONUS (bottom right).

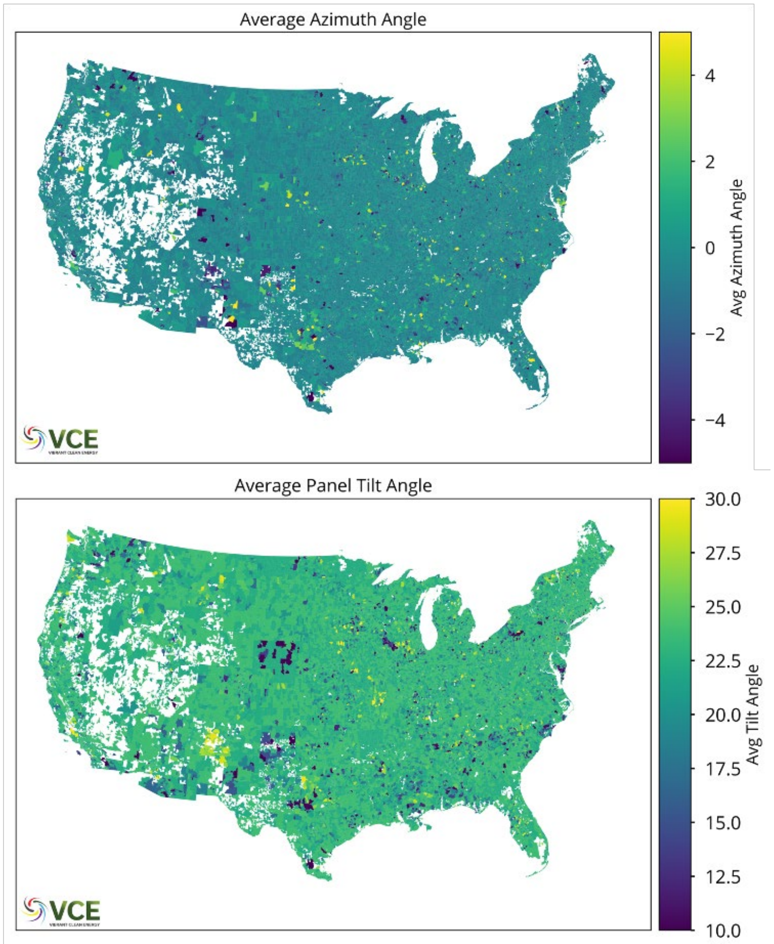

Figure 1.7-B: Average azimuth (top) and tilt (bottom) for each 3-km cell within the WIS:dom®-P model. Areas in white are locations with no available suitable rooftop area.

To accurately calculate expected power production from rooftop solar panels, the azimuth and tilts of suitable rooftop in each 3-km cell are needed. The most accurate dataset containing this information was compiled by the National Renewable Energy Laboratory (NREL) using Light Detection and Ranging (Lidar) measurements of rooftops over the CONUS[2]. Using the lidar measurements, the rooftop azimuth, tilt and rooftop area were calculated.

Shading of the rooftops was determined by running a shading simulation that calculated the number of hours of sunlight received by each square meter of the rooftop over four days: March 21, June 21, September 21, December 21 based on the geometry of the rooftop. Portions of the rooftop that were excessively shaded (more than 20% of the time) were marked as unsuitable. In addition, portions of the rooftop facing northwest through northeast (292.5° to 67.5° from north) were also considered unsuitable. Each rooftop plane with projected horizontal area smaller than 10 m^2 was also excluded.

The buildings in each zip-code were grouped into three categories: small (94% of buildings and 58% of the rooftop area), medium (5% of buildings and 18% of the rooftop area) and large (1% of buildings and 24% of rooftop area). For each of the building category, the tilts were grouped into 5 bins:

---

[2] Gagnon, Pieter; Margolis, Robert; Phillips, Caleb (2019): Rooftop Photovoltaic Technical Potential in the United States. National Renewable Energy Laboratory. https://data.nrel.gov/submissions/121

(1) *flat (less than 9.5° in elevation);*
(2) *15.8° (between 9.5° and 22.1° in elevation);*
(3) *28.4° (between 22.1° and 34.8° in elevation);*
(4) *41.1° (between 34.8° and 47.4° in elevation);*
(5) *53.7° (between 47.4° and 60.0° in elevation).*

The azimuths were also grouped into 5 bins:

(1) *East (between 67.5° and 112.5° from north);*
(2) *Southeast (between 112.5° and 157.5° from north);*
(3) *South (between 157.5° and 202.5° from north);*
(4) *Southwest (between 202.5° and 247.5° from north);*
(5) *West (between 247.5° and 292.5° from north).*

For each zip-code area, the rooftop area weighted azimuth and tilts are calculated. These values are then applied to each 3-km cell within the zip-code region. The resulting average rooftop azimuth and tilts for each 3-km cell are shown in Figure 1.7-B.

1.1.2.2 Estimating power from bi-facial solar photovoltaics

Bi-facial solar PV is included in the solar technologies modeled by VCE®, which are able to increase power production by using irradiance received on the backside of the panel. This increase in power comes at marginally higher cost compared to mono-facial PV panels allowing WIS:dom®-P to determine if the additional generation is worth the increased capital cost. VCE® computed the irradiance received by the backside of a solar panel using the equations from a method provided by NREL[3].

Power production from a bi-facial solar PV panel is calculated similar to a mono-facial panel as described in Section 1.1.2, with the radiation incident on the backside of the panel being added to the radiation incident on the front side of the panel. The frontside irradiance incident on the bi-facial solar PV panel is assumed to be the same as that received by a fixed solar panel with a latitude tilt. The total irradiance incident on the backside of a solar panel (E_{back}) can be calculated as:

$$E_{back} = \sum_{i=Latitude}^{180} CF_i * f_i * \rho * GRI \tag{BF-1}$$

where, *GRI* is irradiance received by the ground, CF_i is the configuration factor for the i^{th} one-degree segment defined as:

$$CF_i = 0.5 * [\cos(\mathrm{i}-1) - \cos(\mathrm{i})]$$

and f_i is the angle of incidence correction for the i^{th} one-degree segment calculated using the polynomial relationship:

$$f_i = b_0 + b_1 * AOI_i + b_2 * AOI_i^2 + b_3 * AOI_i^3 + b_4 * AOI_i^4$$

where, AOI_i is the angle of incidence of the irradiance from the ground on the i^{th} one-degree segment on the back-side of the PV panel and b_0, b_1, b_2, b_3, b_4 are constants. The bi-facial solar PV panels are assumed to be deployed with a tilt equal to the latitude of their siting location. The field of view of the backside of the panel is divided into segments from the panel tilt angle to 180°. This limitation from a full 180-degree view is performed to exclude the portion of irradiance blocked by the solar panel itself. Finally, ρ is the Albedo defined as the ratio of the upward shortwave radiation from the surface versus the downward shortwave radiation

$$\rho = \frac{SW_{up}}{SW_{down}} \tag{BF-2}$$

where, SW_{up} is the shortwave radiation leaving the surface of the earth and SW_{down} is the shortwave radiation received at the surface of the Earth, both in W/m^2. The downward shortwave radiation will dominate, creating a ratio ranging between 0 and 1. A ratio of 0.5 means that 50% of the downward shortwave radiation is being reflected back up from the surface. For surfaces that are snowy, this ratio can easily be over 60%. In general, the albedo is lower in the summertime.

---

[3] B. Marion, S. MacAlpine, C. Deline, A. Asgharzadeh, F. Toor, D. Riley, J. Stein, C. Hansen, "A Practical Irradiance Model for Bifacial PV Modules," National Renewable Energy Laboratory, Presented at IEEE 44th Photovoltaic Specialists Conference, 2017.

The irradiance received by the ground can be calculated using:

$$GRI_n = \alpha * (DNI + I_{cir}) + CF_{sky} * I_{sky}$$

(BF-3)

where, *GRI* is the ground irradiance, *n* denotes the n^{th} segment of the ground between solar panel array rows, α is the cosine of the solar zenith angle, I_{cir} is the circumsolar irradiance, I_{sky} is the Diffuse Horizontal Irradiance (DHI) and $CF_{sky} = 0.5 * (cos\theta_{s1} - cos\theta_{s2})$ is the configuration factor where θ_{s1} is the view angle of the sky blocked by a solar panel in the next row and θ_{s2} is the unblocked view angle of the sky. Since the array layout is unknown, no shading is assumed between PV panel rows. As a result, $\theta_{s1}\ is\ zero$ and θ_{s2} become 180 degrees which results in CF_{sky} to be a factor of 1.

As outputs from a numerical weather prediction model are used to calculate *DNI*, the circumsolar correction is unnecessary (*DNI* calculated from the HRRR is described in Section 4.4.2). In contrast, when using physical measurement devices that measure *DNI*, the circumsolar irradiance would have to be considered and added to the *DNI* separately[4]. As a result, Eq. (BF-3) reduces to:

$$GRI = \alpha * DNI + DHI$$

(BF-4)

From Eq. (BF-4), *GRI* is simply the Global Horizontal Irradiance (*GHI*) measured at the surface. This parameter is calculated as described in Section 4.4.2.

The irradiance on the back-side of the PV panel (E_{back}) calculated from Eq. (BF-1) is added to E_b [Eq. (33) in Section 1.1.2], which gives the total irradiation incident on a bi-facial solar PV panel. The solar power calculation procedure is exactly as described in Section 1.1.2 except the maximum power allowed from the bi-facial panel is limited to 125% of the solar PV panel nominal capacity.

---

[4] P. Blanc *et al.*, "Direct normal irradiance related definitions and applications: The circumsolar issue," *Sol. Energy*, vol. 110, pp. 561–577, 2014.

1.1.3 Temperature power dataset method

Temperature is an important variable in creating the load profiles datasets. Ambient temperatures affect heating (both space and water) and cooling demand, heat rates of conventional generators, transmission losses and ampacity as well as energy use by EVs. Temperature data is available from the HRRR at 3-km spatial resolution and 5-min temporal resolution.

The loads are evaluated at state-level and hourly time-resolution. Therefore, the temperature data needs to be aggregated to state-level, while preserving the spatial variability information present in the original higher resolution dataset. To do this, the temperature data is aggregated to state level by weighting each 3-km HRRR cell by the fraction of the state population in the cell. The population weighting ensures that locations of denser populations get greater weighting on temperatures and hence will have a stronger impact on the demand profile. A similar technique is used to create average temperatures at county level.

1.2 Electric Demand Dataset

The same methods outlined in the present section are applied to all counties and states across the contiguous USA. We provide example state profiles for descriptive purposes and provide a quantifiable example while explaining the concepts for creating the demand datasets.

1.2.1 Traditional demand profiles

State-level hourly loads were developed from FERC 714 data [13]. This database includes hourly load data from grid balancing authorities. Balancing authorities maintain appropriate operating conditions for the electric system by ensuring that a sufficient supply of electricity is available to serve expected demand, which includes managing transfers of electricity with other balancing authorities [14].

The balancing authorities in the database were assigned to states that they most represent and hourly profiles for each of the contiguous US states were developed for 2014 - 2018 by summing the hourly load data for each state. These profiles were then normalized by the annual energy consumption of each state for each year. The process is shown by Equation (35)

$$L_{j,h} = \sum_{i=1}^{n} BA_{i,j,h} \times \frac{L_{j,act}}{\sum_{h=1}^{8760} \sum_{i=1}^{n} BA_{i,j,h}}. \tag{35}$$

Here $L_{j,h}$ is the load for state j at hour h, $BA_{i,j,h}$ is the hourly output for each balance authority i (from the FERC 714 data) associated with state j at hour h (thus, the summation of which equals the calculated hourly load per state), and $L_{j,act}$ is the actual annual load for state j taken from EIA data. The double summation in the denominator of the fraction is simply the estimated annual state load for state j (from the FERC 714 data).

States that were not represented in the FERC database (for lack of a balancing authority or missing data) were assigned to have the same profile as a neighboring state, but were normalized by their own actual annual load.

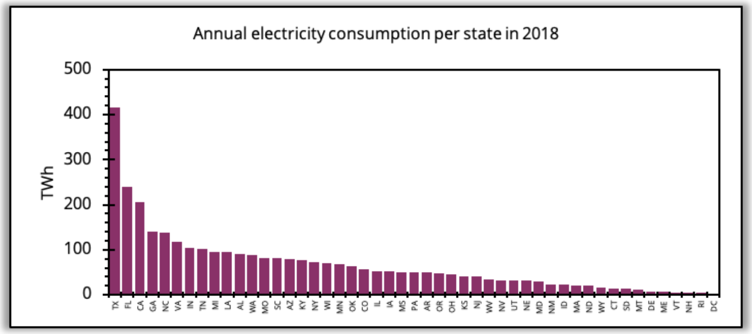

Figure 1.8: Total annual electricity consumption by state for year 2018 generated from FERC 714 data.

Finally, each county was assigned the share of its state load in proportion to its share of the total state population. While there will be differences in counties' load profiles based on their type of load, i.e. heavily industrialized counties will have different load patterns than mostly residential counties, these data simply do not exist in any currently-accessible form.

1.2.2 Space heating demand profiles

Space heating demand depends on local climate and variability in temperature over a year. It is assumed that the ideal indoor temperature (T_{ideal}) for the building stock is 22°C. To calculate flexibility in space heating, it is assumed that the indoor temperature is allowed to drop to 20°C.

The energy rate required to maintain the building stock at T_{ideal} given outside temperature of T_{out} is given by

$$\dot{Q} = H.A.(T_{ideal} - T_{out}) \tag{36}$$

where H is the heat transfer coefficient, and A is the cross-sectional area over which heat transfer occurs.

The value of the heat transfer coefficient varies as function of building material and insulation characteristics, and cross-section area (A) changes depending on size and shape of the buildings. However, assuming these values do not change over the course of the year, they do not need to be explicitly quantified if the fractional energy rate at a given time step is used. The fractional energy rate at a given time step is defined as

$$Q_{ideal}(t) = \frac{H.A.\left(T_{ideal} - T_{out}(t)\right)}{\sum_t H.A.\left(T_{ideal} - T_{out}(t)\right)} \tag{37}$$

$$\Rightarrow Q_{ideal}(t) = \frac{T_{ideal} - T_{out}(t)}{\sum_t \left(T_{ideal} - T_{out}(t)\right)}. \tag{38}$$

The negative values are set to zero (as no heating will be required when outside temperature is above the ideal indoor temperature) before normalizing. The fractional energy rate, when multiplied with the total space heating energy use in a year, gives the energy required for space heating for a given timestep in that year. Figure 1.9 shows fractional energy use profiles for Minnesota and California created for the year 2018.

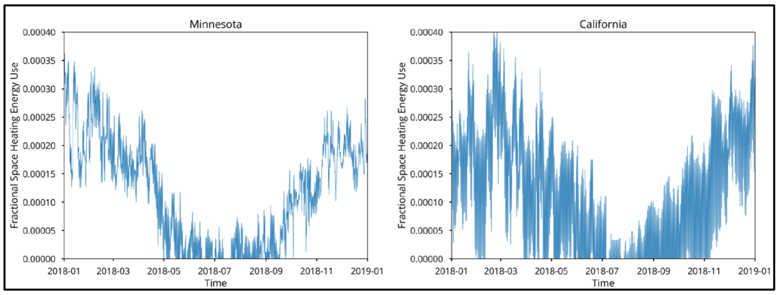

Figure 1.9: Average fraction energy used for space heating in Minnesota and California in 2018. It is observed that in Minnesota there is heating requirements throughout the year, whereas it goes to zero in California during the summer.

It can be seen in Figure 1.9 that Minnesota, which is a colder state, has heating requirement almost all year, while California has zero heating requirements for parts of the summer. It is important to note that although the fractional energy used per timestep in California may be larger in a given hour compared to Minnesota, the actual energy use might be much smaller as these fractional values get multiplied by the annual energy used for heating within that state.

1.2.3 Water heating demand profiles

Water heating is modelled in a similar manner to the space heating. It is assumed that the ideal water temperature to be maintained is 60°C. It is further assumed that the incoming water temperature is correlated to the outside air temperature. Given these assumptions, fractional energy use for water heating at a given timestep is calculated using Eq (38).

Figure 1.10 shows fraction water heating energy use in Minnesota and California. Unlike space heating energy use, it is observed that the profiles for the two states are very similar. The reason for this is that the temperature gradient required to be maintained is so large that the differences in climate is less important. It is, however, observed that energy use at the coldest time in winter is about double the energy use at the warmest time in summer.

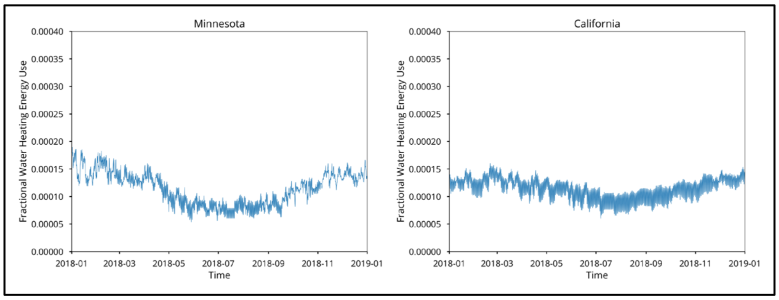

Figure 1.10: Average fractional energy used for water heating in Minnesota and California in 2018.

1.2.4 Space heating flexibility

To calculate flexibility in space heating load, it is assumed that the ideal indoor temperature can be allowed to drop to 20ºC (T_{flex}) for short periods. Therefore, the fractional energy use at each time step assuming temperature is allowed to drop to T_{flex} is:

$$Q_{flex}(t) = \frac{T_{flex} - T_{out}(t)}{\sum_t \left(T_{flex} - T_{out}(t)\right)}. \tag{39}$$

The negative values are set to zero in a similar manner to the space heating calculation. From Equations (38) and (39), the flexibility at each time step can be defined as

$$flex(t) = 1 - \phi \frac{Q_{flex}(t)}{Q_{ideal}(t)}. \tag{40}$$

Here ϕ is a parameter to set the enforced strictness of flexibility. This parameter can be any value between 0 and 1. When $\phi = 1$ the flexibility is at its strictest (fully constrained by ambient outside temperature), while at $\phi = 0$ flexibility is fully available regardless of outside temperature.

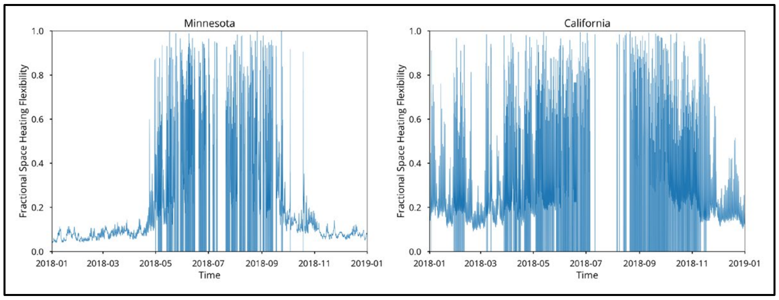

Figure 1.11: Space heating flexibility for Minnesota and California in 2018 for $\phi = 1$.

As seen in Figure 1.11, when space heating demand is very high (see Fig. 1.9) the availability of flexibility is limited in Minnesota during winter because the ambient air temperature is so low that the buildings would cool below the allowed threshold. For California, there is substantial flexibility in space heating for many timesteps during the winter, because the ambient temperatures tend to be much milder. It is also observed that flexibility goes to zero in California in summer. This is due to the fact that no space heating is required during those timesteps and hence there is zero flexibility for space heating load. In colder states, such a Minnesota, space heating needs are present for more time-periods over a year and, thus, there is flexibility associated with that space heating need.

1.2.5 Transportation demand profiles

Energy used by electric vehicles can be broadly divided into two components: Energy used for driving the vehicle and energy used for cabin heating/cooling. Both these components are dependent on weather and have trends that change over the course of a year. In addition, driving habits vary depending on the region and time of the year.

The energy consumed for cabin heating and cooling is given by a modified form of Equation (36) as

$$\dot{Q}_{cabin} = H.A.|(T_{ideal} - T_{out})|, \tag{41}$$

where T_{ideal} is the ideal cabin temperature assumed equal to 22°C and T_{out} is the outside temperature. The absolute value of temperature gradient is used because when outside temperature is too high, cabin cooling takes over from cabin heating, but the energy use is still proportional to the temperature gradient. The fractional energy use for cabin heating or cooling at each time step can now be calculated using an equation similar to (38):

$$Q_{cabin}(t) = \frac{|T_{ideal} - T_{out}(t)|}{\sum_t |(T_{ideal} - T_{out}(t))|}. \tag{42}$$

To calculate the energy used for driving, the driving behavior for each state in the contiguous United States (CONUS) is obtained from the Department of Transport, Office of Highway Policy Information for year 2018. The data is available as monthly averages for the year 2018. The curves are cubic interpolated to create data at each 5-min timestep. The fractional energy use for driving can then be calculated as

$$Q_{drive}(t) = \frac{D_s(t)}{\sum_t D_s(t)}, \tag{43}$$

where, $D_s(t)$ is the miles driven at each timestep.

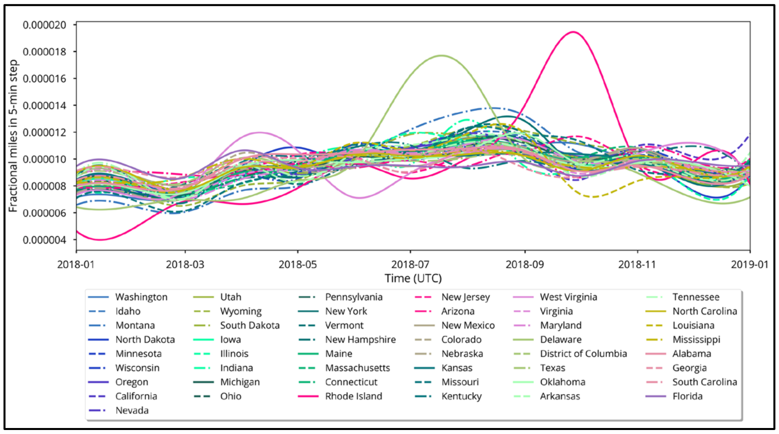

Figure 1.12: Fractional miles driven in a 5-min timestep for each state in the CONUS.

The total energy used by EVs is now a sum of Equations (42) and (43). Since the values are fractional energy use, a multiplier, α (equal to 10%), is applied to Q_{cabin}, which is then added to Q_{drive}. This is done because it is assumed that heating/cooling accounts for about 10% to the total energy used for EVs. Thus, the total fractional energy use is calculated as

$$Q_{total} = \frac{1}{(1+\alpha)}[Q_{drive} + \alpha Q_{cabin}]. \tag{44}$$

The efficiency of running EVs depends on ambient temperatures. The impacts of ambient temperature are (in addition to the cabin heating/cooling) battery internal resistance changes, tire pressure changes, and air density changes. Therefore, the actual energy used by an EV is obtained by multiplying the total energy use by the inverse of the energy efficiency (given by $\eta(t)$ – see Figure 1.13 left panel) due to the ambient temperature at that time step as shown in Equation (45).

$$Q_{actual}(t) = \frac{1}{\eta(t)}\frac{1}{(1+\alpha)}[Q_{drive} + \alpha Q_{cabin}]. \tag{45}$$

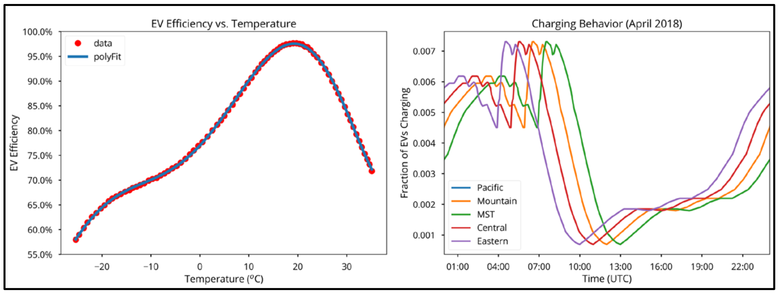

Figure 1.13: Relationship between EV efficiency and temperature (left) and EV charging behavior (right).

The way the EV energy use becomes a load on the grid is when the EV is plugged in to charge the battery. The charging behavior is obtained from a study of charging behavior performed by Idaho National Laboratory in 2013. In this study, a composite profile of all the states studied in the Idaho National Laboratory report at hourly resolution is used. The charging behavior is then adjusted for time-zone (see Figure 1.14) and normalized by the sum of the time series.

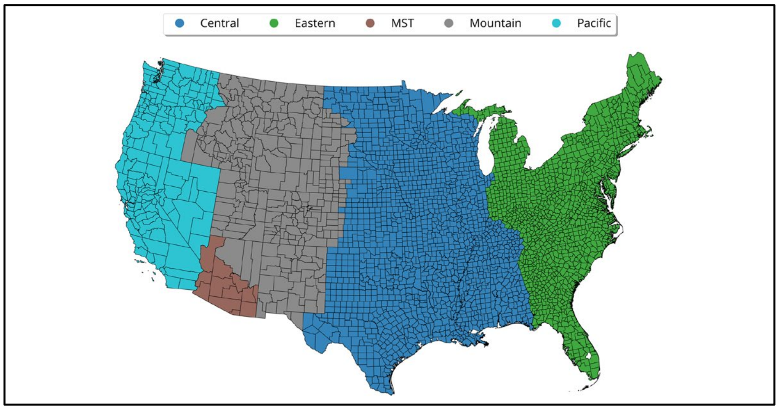

Figure 1.14: Time zones for counties in the CONUS used to localize charging behavior.

The fractional charging behavior is multiplied with the actual EV energy use profile to get the fractional energy demand by EVs at each time step

$$Q_{EV}(t) = C_f(t) * Q_{actual}(t), \tag{46}$$

where C_f is the fractional charging behavior at each time step.

Figure 1.15 shows fractional transportation electricity demand profiles in Minnesota and California. The shape of the electricity demand profile in Minnesota resembles the shape of the heating energy use. The reason for this is that the cold weather in Minnesota increases energy use for heating the cabin, while dealing with lower energy efficiency, which results in much higher electricity demand in winter than in summer. Whereas, the California transportation electricity demand profiles show much better correlation with the driving behavior. This points to the milder climate in California.

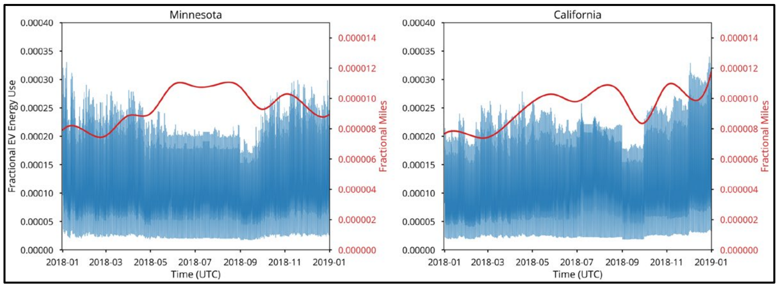

Figure 1.15: Fractional EV energy use for two states for 2018. The relative importance of efficiency and energy use as function of temperature compared to driving behavior is clearly seen.

1.3 Removing Space, Water Heating and Transport from Historical Electricity Use

WIS:dom® uses historical load data from FERC form 714 to create the basis for the demand curves as explained in Section 1.2. The historical data contains contributions from demand for space heating, water heating and EV energy use. To enable modeling demand from space heating, water heating and transport separately, they need to be removed from historical energy use numbers to avoid double counting the demand.

The total demand is given by:

$$D_{total}(t) = A_{conv}N_{conv}(t) + A_{(spHeat)}N_{spHeat}(t) + A_{wHeat}N_{wHeat}(t) + A_{EV}N_{EV}(t) \qquad (47)$$

where, $D_{hist}(t)$ is the historical demand curve, A_{conv} is the annual conventional demand, $N_{conv}(t)$ is the normalized conventional demand curve at hourly resolution, A_{spHeat} is the annual space heating demand, $N_{spHeat}(t)$ is the normalized space heating demand curve at hourly resolution, A_{wHeat} is the annual water heating demand, $N_{wHeat}(t)$ is the normalized water heating demand curve at hourly resolution, A_{EV} is the annual demand for EV, and $N_{EV}(t)$ is the normalized EV demand curve at hourly resolution.

Since the FERC data does not split the demand out into categories, the historical demand obtained from FERC is given by:

$$D_{hist}(t) = \left(A_{conv} + A_{spHeat} + A_{wHeat} + A_{EV}\right) * N_{hist}(t) \qquad (48)$$

where, $D_{hist}(t)$ is the historical demand curve from FERC form 714 and $N_{hist} = {}^{D_{hist}}\!/_{\sum_t D_{hist}(t)}$ is the normalized historical demand curve at hourly resolution.

The normalized historical demand curves for Minnesota and California are shown in Figure 1.16.

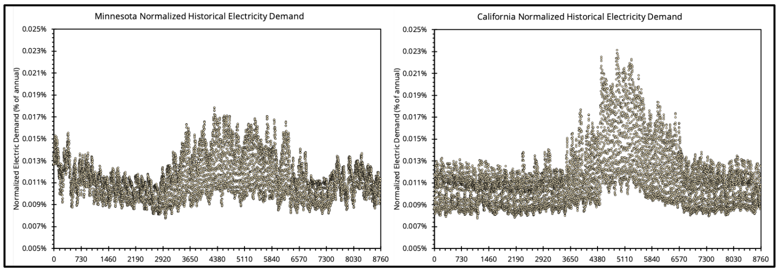

Figure 1.16: Normalized historical demand curves calculated from FERC form 714 for Minnesota (left) and California (right).

Since, the historical demand is equal to the total demand at model initialization, the adjusted normalized conventional demand, which removed contributions from space heating, water heating and transport can be calculated using Equations (47) and (48) by:

$$N_{conv}(t) = \frac{1}{A_{conv}}\begin{bmatrix} \left(A_{conv} + A_{spHeat} + A_{wHeat} + A_{EV}\right) * N_{hist}(t) \\ -\left(A_{spHeat}N_{spHeat}(t) + A_{wHeat}N_{wHeat}(t) + A_{EV}N_{EV}(t)\right) \end{bmatrix} \qquad (49)$$

The adjusted normalized conventional demand curve calculated using Equation (49) is shown in Figure 1.17. It is observed that the winter periods show a smaller fraction as the space heating contributions are removed and the summer portion of the curve show larger fractions as they make up a larger portion of the energy use.

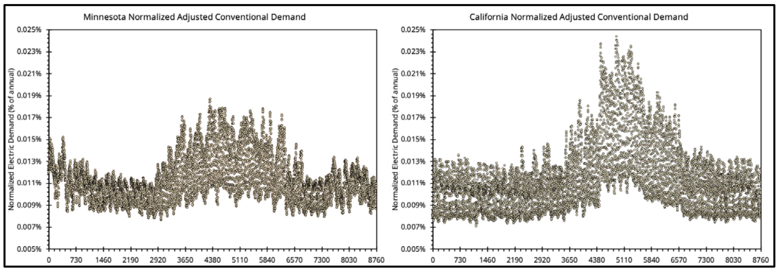

Figure 1.17: Adjusted normalized conventional demand curves after removing contributions from space heating, water heating and transport for Minnesota (left) and California (right).

1.4 Transmission Line Rating & Electric Losses Dataset

As ambient temperatures increase, transmission lines are less able to reject heat generated due to resistive heating of the transmission lines. As a result, a decision has to be made on whether to operate the transmission line at a higher temperature (which increases losses) while keeping the full rating or to de-rate the transmission capacity to prevent damage to the conductor or the surroundings due to the sag of the transmission line. WIS:dom® models the transmission lines assuming steady state energy balance, where heat gained due to resistive heating ($q_{current}$) and solar irradiance ($q_{solarIrr}$) equals heat lost due to convective heat transfer ($q_{convHeatTransfer}$) and radiative heat transfer ($q_{radiativeHeatTransfer}$) as

$$q_{current} + q_{solarIrr} = q_{convHeatTransfer} + q_{radiativeHeatTransfer}. \tag{50}$$

Resistive heating is given by

$$q_{current} = I^2 R(T_{cond}), \tag{51}$$

where, I is the current in the transmission line, and $R(T_{cond})$ is the resistance of the transmission line which itself is a function of conductor temperature (T_{cond}). The resistance of the conductor is related to the conductor temperature by

$$R(T_2) = R(T_1) * [1 + \alpha(T_2 - T_1)], \tag{52}$$

where, α is a constant with a value of 0.0039 and T_1 and T_2 are the initial and final temperatures of the conductor.

Heating due to solar irradiance is calculated assuming the conductor is a black body and can be calculated using

$$q_{solarIrr} = \delta * \pi D * a_s, \tag{53}$$

where, δ is the downward short-wave solar radiation in W/m^2, D is the diameter of the conductor, and a_s is the absorptivity of the conductor (assumed to be 0.9).

The convective heat transfer from the conductor to its surroundings is given by

$$q_{convHeatTransfer} = h * \pi D * (T_{cond} - T_{air}). \tag{54}$$

Here, h is the convective heat transfer coefficient given by

$$h = Nu * {}^{k}\!/_{D}, \tag{55}$$

where, Nu is the Nusselt number and k is the thermal conductivity of air in W/m-K.

The Nusselt number can be calculated using

$$Nu = 0.3 + \frac{a}{b}(1 + c)^{4/5}, \tag{56}$$

where, $a = 0.62 * Re^{1/2} * Pr^{1/3}$, $b = \left[1 + \left(\frac{0.4}{Pr}\right)^{2/3}\right]^{1/4}$, $c = \left(\frac{Re}{282{,}000}\right)^{5/8}$, $Re = V * {}^{D}\!/_{\nu}$ is the Reynold's number, *Pr* is the Prandtl's number, *V* is the wind speed, and ν is the dynamic viscosity.

The heat lost from the conductor due to radiative heat transfer is calculated using

$$q_{radiativeHeatTransfer} = \varepsilon * \sigma * \pi * D * (T_{cond}^4 - T_{air}^4), \tag{57}$$

where, ε is the emissivity of the conductor (assumed to be 0.7) and σ is the Stefan-Boltzman constant equal to 5.67E-8 W/m^2-K^4.

Using Equations (50) - (57), the allowable current to maintain a given conductor temperature (T_{cond}) is given by

$$I = \sqrt{\frac{\pi * h * D * (T_{cond} - T_{air}) + \pi * \varepsilon * \sigma * D * (T_{cond}^4 - T_{air}^4) - \delta * \pi * D * a_s}{R(T_{cond})}}. \tag{58}$$

The current method for computing the high-temporal (dynamic) transmission line rating assumes that each transmission line is already appropriately rated based on yearly average local weather conditions. It is then determined what the up- and down- rating should be applied to safely utilized the transmission line. Therefore, Equation (58) is used to calculate the maximum current that can be sent through a transmission line while maintaining an ideal conductor surface temperature of 75°C. Once the allowable current values are calculated, the current values are normalized by the average current value for the CONUS over the year, which gives the fractional dynamic line rating for each timestep over the year.

From the above method of determining the fractional dynamic transmission line rating, there will be periods (usually in winter) where the transmission rating will be greater than unity and periods (usually in summer) where it will be less than unity. A secondary step is now added to the method, where it is assumed that when the fractional dynamic transmission line rating is less than unity, the conductor temperature can increase up to 95°C in order to try and increase the fractional dynamic transmission line rating back to unity. The conductor temperature can be calculated using Equation (55) by iteratively increasing conductor temperature until a fractional dynamic transmission line rating of unity is achieved. If the conductor temperature reaches 95°C before the fractional dynamic line rating reaches unity, no further increase in temperature is allowed. Thus, some periods will have a fractional dynamic line rating that is less than unity since it is no longer safe to increase the fractional dynamic line rating.

An additional constraint imposed is that the temperature gradient between the conductor core and its surface is not allowed to exceed a safe value (IEEE recommended value is 10°C). The temperature gradient between the conductor surface and its core can be calculated using

$$T_{core} - T_s = \frac{I^2 R\left(T_{avg}\right)}{4\pi k_{th}}, \tag{59}$$

where T_{core} is the conductor core temperature, T_s is the conductor surface temperature, k_{th} is the thermal conductivity of the conductor material, $R(T_{avg})$ is the conductor resistance at the average temperature of the surface and core.

Since the calculations performed here are relative, the safe temperature gradient is determined by using the average temperature gradient observed during periods of fractional dynamic line rating greater than unity. The line ratings are then re-calculated to ensure this temperature gradient is not exceeded.

The final conductor temperatures obtained from the above procedure are used to calculate the change in dynamic transmission line electric losses. The dynamic transmission line electric losses depend on the current passing through the conductor as well as its resistance. The resistance of the conductor is a function of temperature as given in Equation (52), while at higher conductor temperatures, the transmission line is de-rated to send lower current through the line. Therefore, the dynamic transmission electric losses is calculated using

$$Loss_{change} = \frac{I(t)^2 R(t)}{I_{avg}^2 R(75^o C)}, \tag{60}$$

where, $I(t)$ is the current rating of the conductor at each timestep calculated from Equation (58), $R(t)$ is the resistance at each timestep calculated using Equation (52), I_{avg} is the average current rating of the conductor, and $R(75^oC)$ is the resistance of the conductor at 75°C.

Equation (60) shows that the dynamic transmission line electric losses are proportional to the square of the current flowing through the conductor and directly proportional to the change in resistance, which increases linearly with conductor temperature. As a result, during colder periods, more current will be flowing through the transmission lines (due to the dynamic transmission line rating being greater than unity) and, hence, will have larger dynamic transmission line electric losses even though the resistance will be lower. Whereas, in hotter periods, the transmission line will be de-rated, so transmission line electric losses will be lower although the resistance of the conductor is higher. There will be variations to this behavior depending on the amount on derating/uprating and change in conductor temperature.

It is important to note that this method of determining fractional dynamic transmission line rating is designed to be relative and not absolute. The method assumes that transmission lines are already rated for the yearly average local weather conditions. Starting from that assumption, it is determined how much uprating/derating results from requiring that the transmission line is used to its maximum potential while ensuring safe operational conditions.

Figure 1.18 shows the fractional dynamic transmission line rating and dynamic transmission line electric losses for Minnesota and California. While California has lower fractional dynamic transmission line rating compared to Minnesota due to its warmer weather, it has less variability in transmission rating changes due to its lower inter-seasonal variability in temperature. For Minnesota, the dynamic transmission line electric losses show a similar pattern as the fractional dynamic transmission line rating because the losses are proportional to the square of the current passing through the conductor and hence the change in current dominate in the changes to the losses. It is further observed from Figure 1.18 (bottom panel) that change in losses in California are less correlated with changes in transmission rating. The is due to the smaller variability in transmission rating in California resulting in smaller changes to the current, which makes them on the same order as changes to the resistance of the conductor.

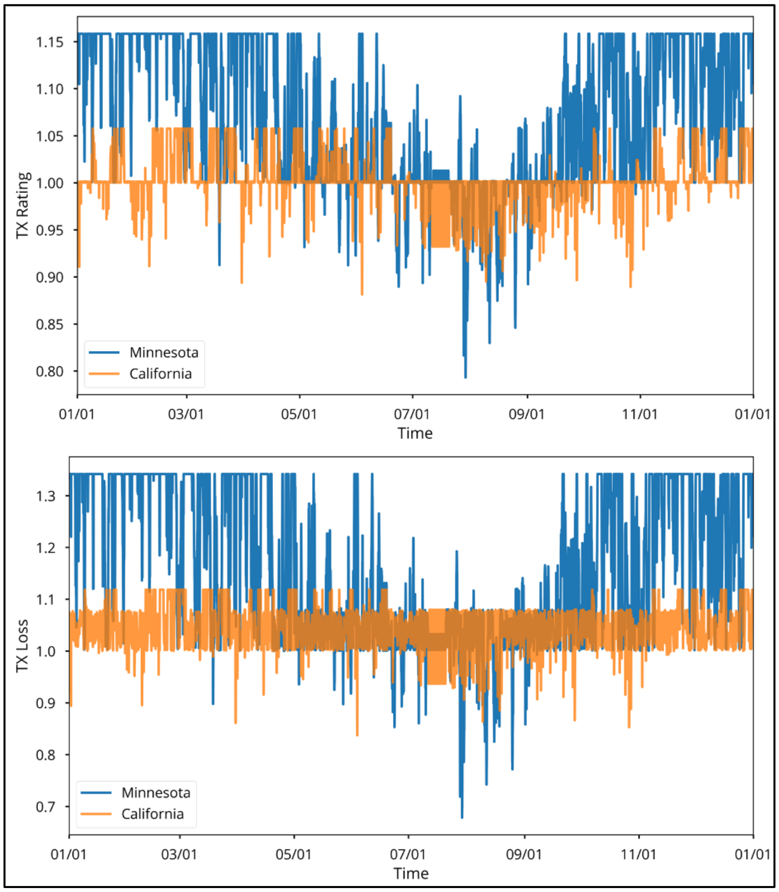

Figure 1.18: Fractional dynamic transmission line rating (top) and fractional dynamic transmission line electric losses (bottom) for Minnesota and California.

The fractional dynamic transmission line ratings and electric losses exhibit the expected patterns for the CONUS as seen in Figure 1.19. It is observed that warmer regions of the CONUS such as the south-east and the south-west have lower than average fractional dynamic transmission line ratings (and consequently, lower average fractional dynamic transmission line electric losses). Meanwhile the Midwest and central portions of the CONUS have higher than average fractional dynamic transmission line rating (and consequently higher average fractional dynamic transmission line electric losses).

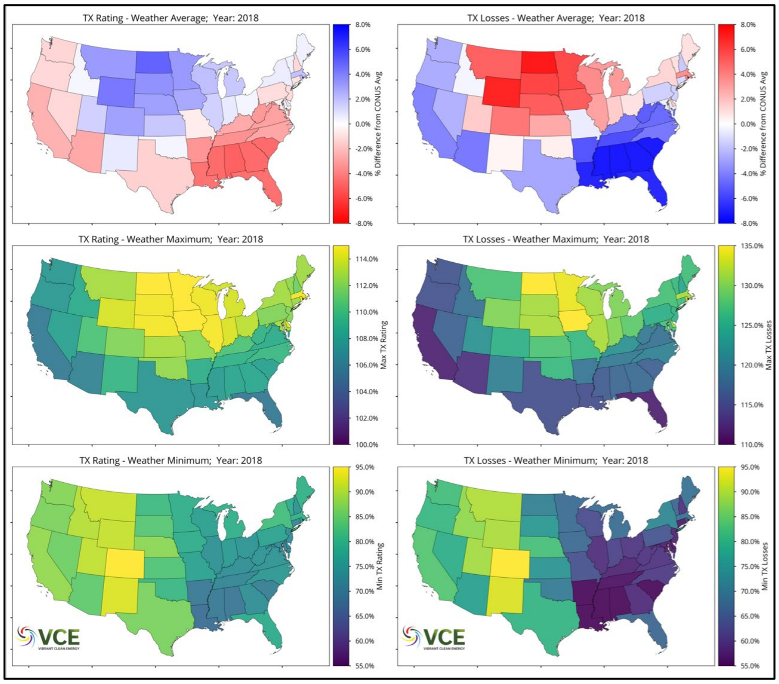

Figure 1.19: Average fractional dynamic transmission line rating (left) and electric losses (right) for the CONUS for weather year 2018. Top panels show deviation of line rating and electric losses from the CONUS average, middle panels show the maximum line rating and losses, and the bottom panels show the minimum line rating and losses.

Looking at the maximum line rating for the year (middle panel), it is observed that the higher than average line ratings in the Midwest are driven mostly by the higher maximum line ratings possible in those states (as these states also tend to have lower minimums). It is also observed that states with lower than average line ratings show a smaller spread between in their maximum and minimum values.

1.5 Climate Change Dataset

Anthropogenically driven climate change creates changes in mean meteorological parameters such as wind speed, solar irradiance reaching the surface, precipitation, temperature and so on. Changes in these meteorological parameters result in alterations in the performance of wind turbines, solar PV cells, conventional power plants (through heat rates and water availability) and transmission line ratings and losses on the generation side. On the demand side, the changes due to climate will result in shifts to the heating and cooling loads, available flexibility, and EV energy use.

WIS:dom® models the impact of climate change on both the demand side and generation side. The United Kingdom Meteorological (UK Met) climate model, HagGEM2-ES, results from CMIP5 are used to estimate the changes in various meteorological variables affecting energy generation and demand. WIS:dom® updates the impact of climate change on the meteorological variables at each investment period, which occurs every 5 years. As a result, effects of large-scale climate cycles, such as El Nino/La Nina, can create large variations depending the year chosen as investment period. To reduce the variability introduced through these large-scale climate cycles, the meteorological variables from the climate models are smoothed using a 5-year moving window. Figure 1.20 shows the change in surface temperature for two Representative Concentration Pathway (RCP) scenarios after applying the 5-year moving average. The impact of climate change on surface temperatures is clearly seen. In the RCP 4.5 scenario, it is observed that more temperature increases are seen in the winter months compared to the summer while in the RCP 8.5 scenario, higher temperature rises are observed in the summer and extends warmer weather to later parts of the year.

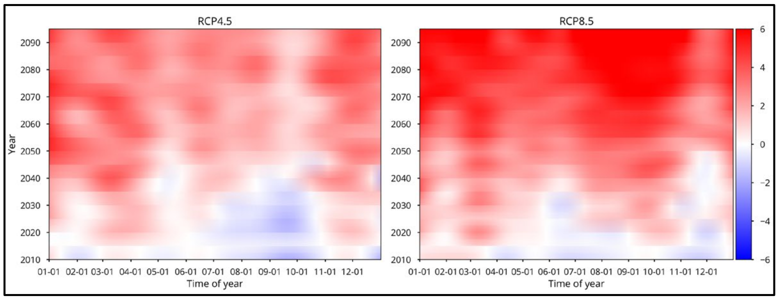

Figure 1.20: Change in average temperature over the CONUS over the course of a year out to 2100.

The following subsections describe how the climate change impacts each aspect of generation and demand within the WIS:dom® modeling framework.

1.5.1 Changes to wind energy production potential

The CMIP5 model data that VCE® has access to only provides monthly mean wind speed at 10 m. Therefore, the monthly mean 80 m wind speed is estimated using a power law assuming a power law coefficient of 1/7 (commonly found for neutral boundary layers). The monthly means can be used to create Weibull distributions of wind speed for that month. The Weibull distributions are created assuming a shape factor (*k*) of 2, which is commonly found to be the case, and by calculating the scale factor using

$$c = \frac{2 * v_m}{\sqrt{\pi}}, \tag{61}$$

where v_m is the monthly mean wind speed at 80 m.

Once the shape and scale factors are determined, the estimated wind energy production within that month can be determined using

$$P_{est} = 0.5 * \rho * A * C_p * \sum_{v=0}^{25} v^3 * f(v). \tag{62}$$

The estimated wind energy production is calculated for every year from 2010 to 2100. Now, the change in wind energy production with respect to the reference year (2018 in this case) can be calculated. The change in wind energy production is now estimated at monthly resolution from 2010 to 2100. The monthly change in wind energy production is cubic spline interpolated to hourly resolution, which is used to nudge the wind power capacity factors described in Section 2.

Changes in expected wind power over the CONUS show significant spatial variability in both the climate RCP scenarios as seen in Figure 1.22. In RCP 4.5, an increase in expected wind power is forecasted over the great plains and most of the western part of the CONUS. However, in RCP 8.5, larger increases in wind power are forecasted in smaller regions, such as the southeast and the southern great plains, while the northern and western parts of the CONUS show a reduction in expected wind power.

It is observed from Figures 4.69 and 4.70 that available wind power over the CONUS under both climate scenarios shows significant variability year over year with a generally positive trend. It is unclear whether this increase in wind power is observed due to higher wind speeds observed from increased storm and hurricane activity. The significant variability observed between each 5-year period shows the challenge that might face wind developers as there would be substantial uncertainty on the performance of the wind farms which would be difficult to plan for. In addition, locally suitable sites might become undevelopable.

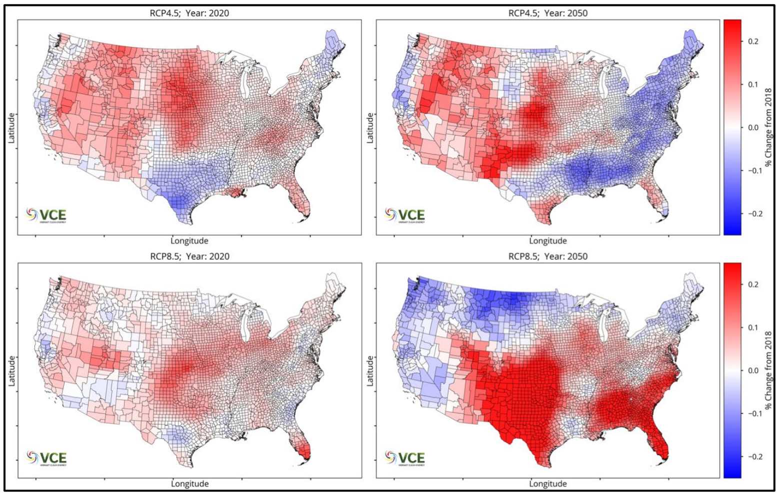

Figure 1.21: Change in wind power due to climate change in the RCP 4.5 scenario for 2020 (top left) and 2050 (top right) and in RCP 8.5 scenario for 2020 (bottom left) and 2050 (bottom right).

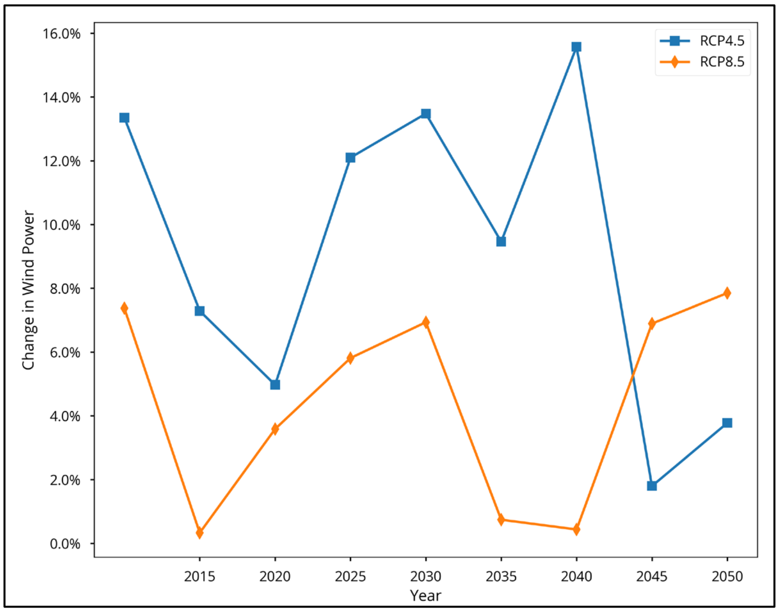

Figure 1.22: Average change in wind power potential over the CONUS under the RCP 4.5 and RCP 8.5 scenarios.

1.5.2 Changes to solar PV energy production potential

As anthropogenic climate change progresses, it is observed that solar irradiance reaching the surface increases marginally due to dryer weather conditions. This increase in solar irradiance reaching the surface should increase power generation from solar panels. However, the ambient temperatures also increase. This increase in ambient temperatures makes solar panels less efficient with about 1% drop in efficiency observed for every 1ºC increase in temperature [12]. Both these effects are modelled by VCE® to account for the impact of climate change on solar power generation potential.

Figure 1.23 shows that in the RCP 4.5 scenario, there is increase in solar irradiance in both the southwest and the southeast, however these are accompanied by increases in temperature and as a result there is a net reduction in the expected solar power potential (Figure 1.24). In the RCP 8.5 scenario, solar irradiance increases in the southeast, and is accompanied by larger increases in temperature in those regions as well.

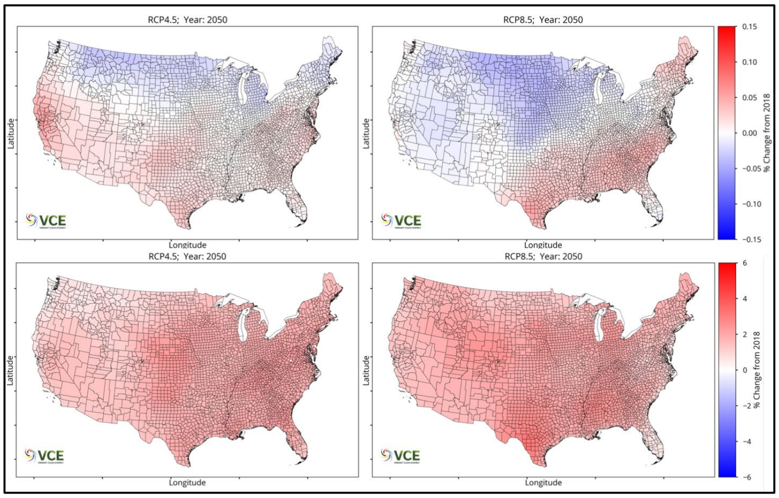

Figure 1.23: Change in solar irradiance reaching the surface in 2050 for climate scenario RCP 4.5 (top left) and RCP 8.5 (top right) compared to 2018 and change in 2-m temperature in 2050 in climate scenario RCP 4.5 (bottom left) and RCP 8.5 (bottom right).

It is observed that the combined effect of the change in solar irradiation and 2-m temperatures is to reduce the solar power generation by 2050 as displayed in Figure 1.24. The reduction in RCP 8.5 scenario is larger (about 2.5%) compared to the RCP 4.5 scenario (about 1.1%). The lower reductions in RCP 4.5 scenario is most probably due to the lower temperatures observed in that scenario, which enables higher solar PV cell efficiencies compared to those observed in the RCP 8.5 scenario.

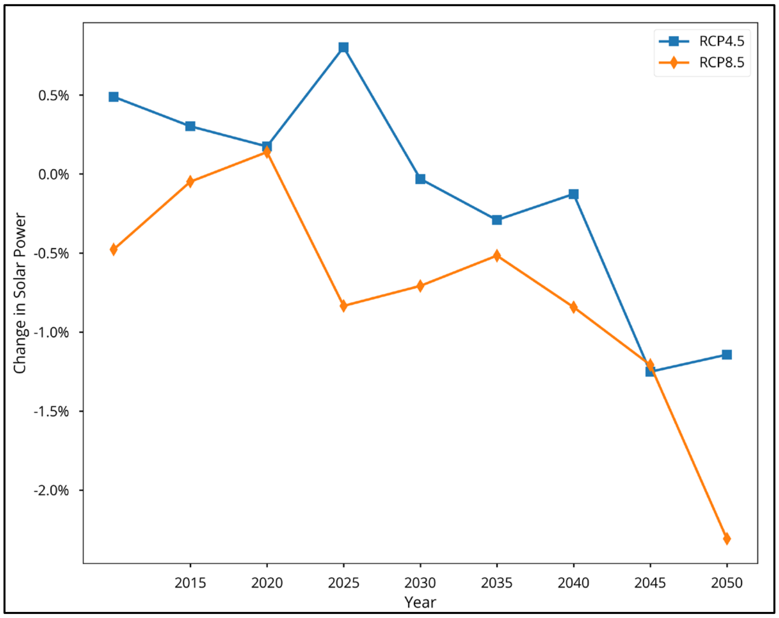

Figure 1.24: Change in solar power output based on changes in temperature and solar irradiance for the two climate scenarios.

1.5.3 Changes to thermal generator heat rates & water

Anthropogenic climate change impacts generation from thermal generators as well as weather-driven generators. Higher ambient temperatures result in less efficient operation of the thermal generators in form of higher heat rates. In addition, conventional generators are affected by access to water which depends on changes in precipitation observed in the two climate scenarios. As seen within Figure 1.25 (left panel), heat rates go up on an average by 2.8% in RCP 8.5, while in RCP 4.5 they go up by about 2.5%. The change in precipitation (Figure 1.25 right panel) is much more variable with year-on-year changes on the order of 20% in both climate scenarios. This indicates the additional uncertainty imposed on the operation of the thermal generators, which could lead to unplanned downtimes due to lack of access to water.

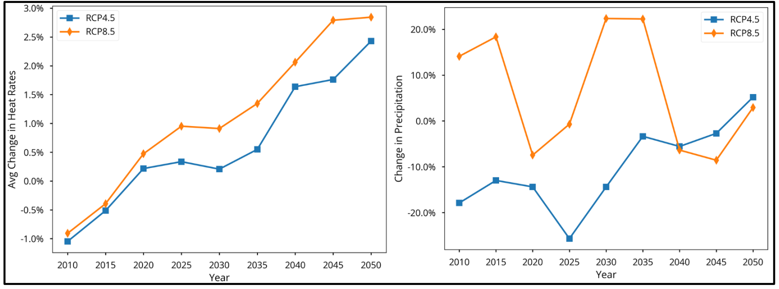

Figure 1.25: Average changes in heat rates (left) and precipitation (right) over the CONUS as a result of climate change for the two RCP scenarios.

An important aspect of the changes to the heat rates is the timing of their occurrence. During any given year, heat rates are their highest in summer due to the higher ambient temperatures. Figure 1.26 shows that the effect of climate change is to increase the summer peak heat rates even further. It is observed that in the RCP 4.5 scenario, heat rates are increased in winter and summer, while in the RCP 8.5 scenario, just the summer peak is seen to increase. This trend correlates to the temperature changes due to climate change (as shown in Figure 1.20), where the RCP4.5 scenario forecasts increased temperatures in winter and summer, while in RCP8.5 scenario, larger increases are seen in summer and extension of the summer period.

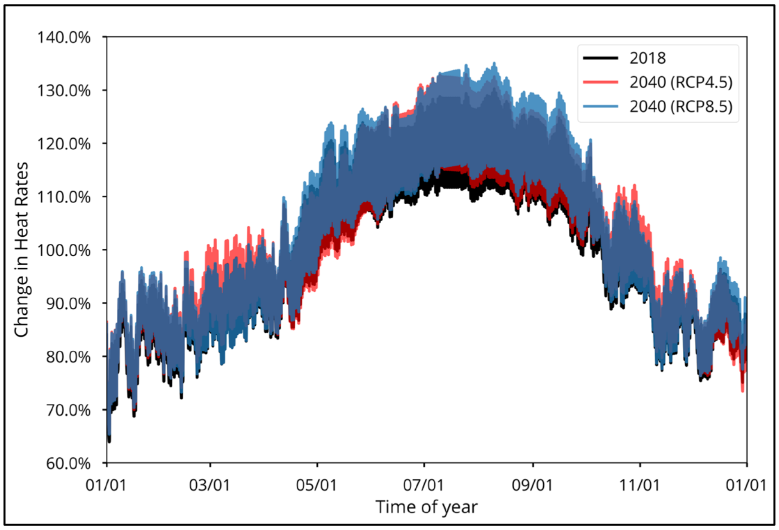

Figure 1.26: Change in heat rates, compared to the yearly averaged value, over the course of a year and impact of climate change in the two RCP scenarios.

1.5.4 Changes to line ratings & electric losses

As ambient temperatures increase due to climate change, the transmission lines will need to be de-rated to prevent excessive heating of the conductor. Some of this effect might be mitigated due to the increase in wind speed predicted by the climate models. The transmission line rating under climate stress is estimated using the climate data to calculate the allowable current in the conductors using Equation (55) and (56), however, it is normalized by the average current calculated for the CONUS using the 2018 weather data. The line ratings are then adjusted as before to ensure that the periods below a rating of unity are adjusted upward without exceeding safe operating maximum temperature of the conductor and the maximum allowable temperature gradient between the conductor core and the surface. The changes to the transmission electric losses are calculated by using the new conductor temperatures and current under influence of climate change stress and using Equation (57) to determine the new loss term.

As can be seen in Figure 1.27, there is a maximum reduction of about 1% in transmission line rating and approximately 2% reduction in transmission line losses averaged over a year in RCP 8.5 scenario, while there is about2% reduction in line rating and 3% reduction losses in RCP 4.5 scenario. The larger reduction observed in the RCP 4.5 scenario is mainly due to smaller increases in wind speeds forecasted in RCP 4.5 scenario, which have a larger adverse effect that the larger temperature increases forecasted in RCP 8.5 scenario.

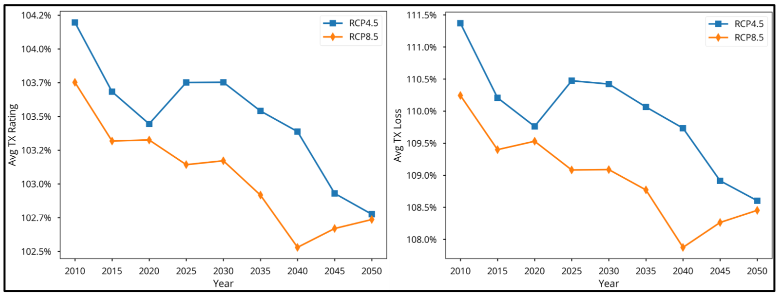

Figure 1.27: Change in transmission line rating (left) and losses (right) due to increase in ambient temperatures due to the effect of climate change.

Similar to heat rates, the change in transmission line rating and electric losses show seasonal trends. Figure 1.28 shows the change in CONUS average transmission line rating and electric losses over a year for weather year 2018 (black line), climate scenario RCP 4.5 (red line) and climate scenario RCP 8.5 (blue line). It is observed that RCP 4.5 shows higher line ratings and electric losses in the winter periods, which is mainly due to the RCP 4.5 scenario forecasting an increase in winter wind speeds compared to 2018. Meanwhile in RCP 8.5 scenario, the winter wind speeds are forecasted to decrease compared to 2018, which combined with the ambient temperature increase results in a significant reduction in line ratings (and consequently electric losses) in the winter. Both climate scenarios predict a decrease in the summer time transmission line rating and electric losses compared to 2018 values.

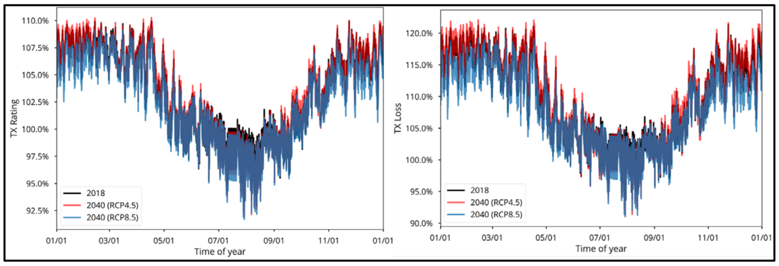

Figure 1.28: Change in transmission line ratings (left) and electric losses (right) compared with the 2018 yearly average value.

The change in transmission line rating and electric losses due to climate change are most sensitive to change in ambient temperatures and wind speeds. Figure 1.29 shows the changes in transmission line ratings (left panels) and electric losses (right panels) in RCP 4.5 (top panels) and RCP 8.5 (bottom panels) scenarios. It is observed in RCP 8.5 scenario that wind speeds decrease over the northern part of the CONUS and increase over the southern parts, while the temperatures are seen to increase more over the southern parts of the CONUS compared with the northern parts. As a result, the temperature increases in the southern parts of the CONUS are mitigated by the higher wind speeds and result in lower derating compared to the northern parts of the CONUS in RCP 8.5 scenario.

As explained previously, the transmission electric losses are more sensitive to the change in current rating of the conductors than change in resistance. This behavior is evident in the Midwest and a few north-western states. However, it is observed that the southeast and southwest states show an increase in losses although there is a reduction in the line rating. The reason for this is that they have a lower reduction in line rating (due to increased wind speeds) combined with a larger increase in ambient temperatures that lead to having higher electric losses.

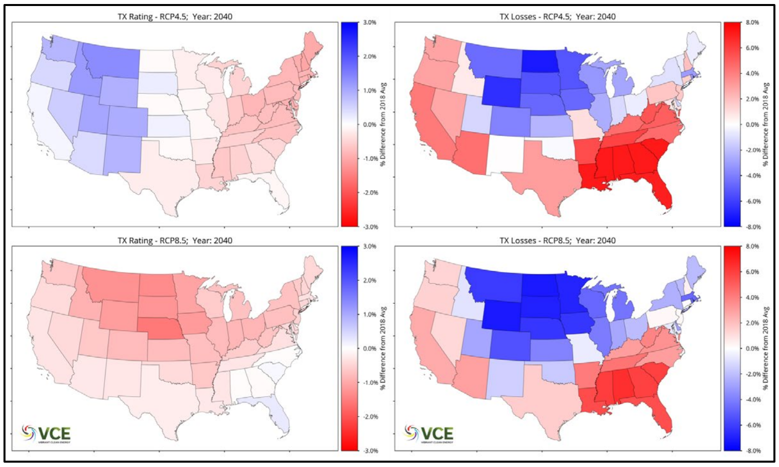

Figure 1.29: Impact of climate change on transmission line rating (left) and electric losses (right) for RCP 4.5 (top) and RCP 8.5 (bottom) scenarios.

1.5.5 Changes to space heating demand

As seen from Equation (38), increasing ambient temperatures (due to climate change) reduces the amount of energy required to maintain the ideal indoor temperature for the building stock. It is observed that the total reduction in energy required for space heating over the CONUS reduces by 8.2% for RCP 8.5 and by about 7.5% for RCP 4.5 (see Figure 1.30) due to the increase in ambient temperatures.

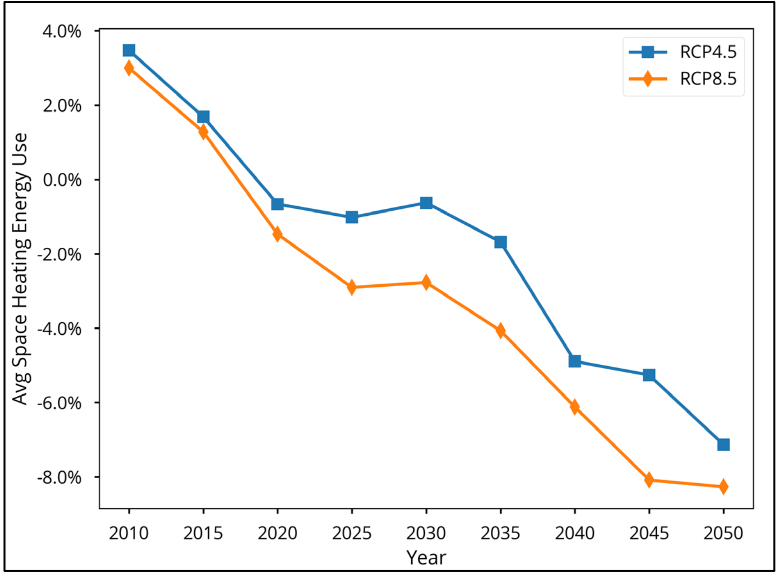

Figure 1.30: Change in space heating energy requirements over the CONUS in the two RCP scenarios.

In addition to the amount of reduction in the space heating load, it is important to know when the reduction is taking place. Figure 1.30 shows the average fractional space heating energy consumption for the CONUS in 2018 and in 2050 for the two RCP scenarios. It can be seen that in the RCP 4.5 scenario, there is a reduction in energy needed during the winter months as well as during the summer months. Whereas in the RCP 8.5 scenario, the reductions occur in the spring and summer season. As explained before, this trend is due to the differences in the timing of the temperature increases forecasted in the two RCP scenarios. The variability in the timing of the change in energy use can have important consequences on how WIS:dom® resource decisions are made.

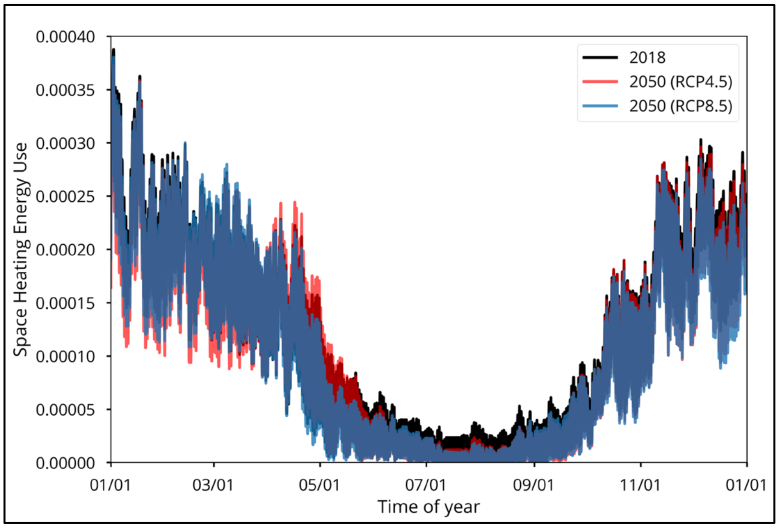

Figure 1.31: Fractional space heating energy use over the course of a year in the two RCP scenarios compared with 2018.

1.5.6 Changes to water heating demand

Impact on water heating is quite small due to the fact that the temperature gradient required to be maintained is large and hence smaller increases in ambient temperature due to climate change do not result in significant change to the energy requirements. The changes observed are similar to those observed for space heating (shown in Figure 1.32), where the RCP 4.5 scenario predicts lower energy usage during the winter and summer, while the RCP 8.5 scenario predicts lower energy usage in spring and summer.

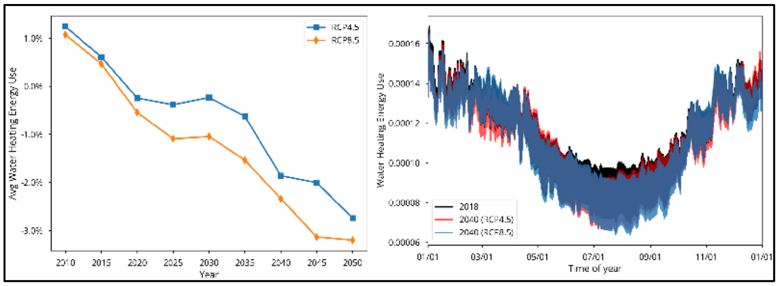

Figure 1.32: Change in fractional water heating energy use due to RCP change compared with 2018.

1.5.7 Changes to conventional & cooling demand

Energy use for space cooling is calculated in a similar manner to space heating energy use by assuming ideal indoor temperature as 22°C and using Equation (63) to calculate fraction energy use at each timestep

$$Q_{ideal}(t) \; = \frac{T_{out} - T_{ideal}(t)}{\sum_t \left(T_{out} - T_{ideal}(t)\right)}. \tag{63}$$

The fractional energy use is calculated at hourly time resolution for the whole US for each of the years for the two climate scenarios. Next, the change in cooling energy use for each timestep is calculated with respect to year 2018. Figure 1.33 shows the change in space cooling energy use for the CONUS in the two climate scenarios. It is observed that there is about a 16% increase in energy use for cooling in RCP 8.5 and about 13% increase in RCP 4.5.

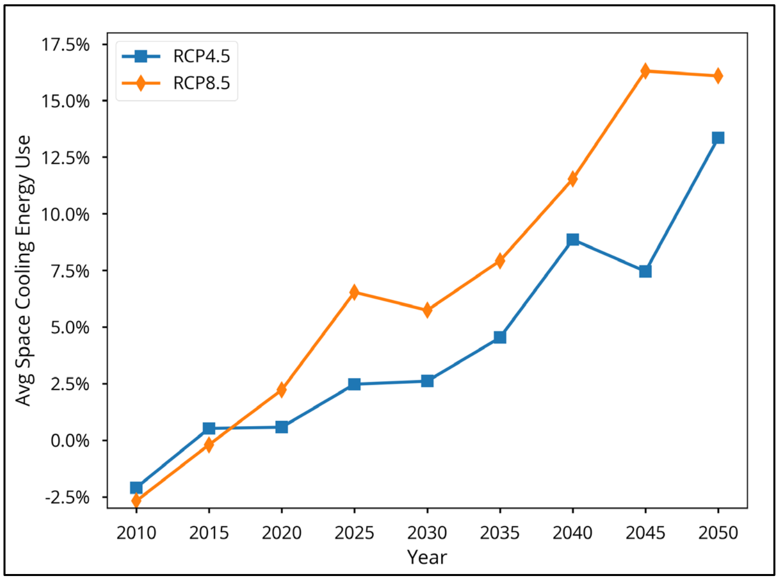

Figure 1.33: Change in space cooling energy use over the CONUS for the two RCP scenarios.

In addition to the magnitude of the increase, the timing of increase in energy use is important in determining how the demand profile changes. Figure 1.34 shows the change at each hourly timestep for all the years in the two climate scenarios. As it would be expected, the largest positive changes occur during the summer in both climate scenarios. It is observed that in RCP 8.5 scenario the increase in energy use occurs over larger portion of the year. While in the RCP 4.5 scenario, there is a reduction in space cooling energy use during spring and fall as the temperatures are forecasted to remain mild during those periods in the RCP4.5 scenario.

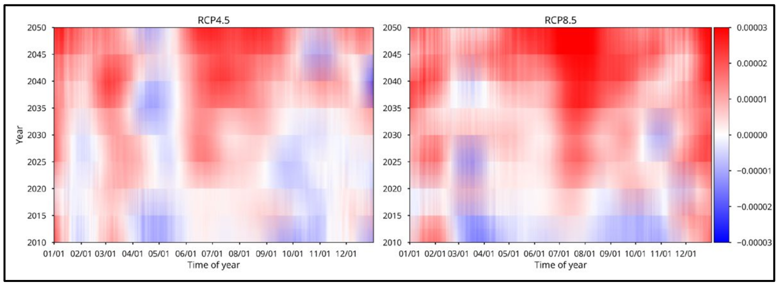

Figure 1.34: Fractional change in each hourly timestep in space cooling demand for the CONUS due to impact of climate change.

1.5.8 Changes to transportation demand

The transportation energy use has complicated interaction effects due to impact of climate change. The increasing temperatures reduce the need for heating in the winter while also increasing efficiency as milder winters improve battery performance. Whereas, in summer cooling needs increase thereby increasing energy use and, in addition, efficiency drops once the temperatures rise above the peak efficiency temperature (see Figure 1.36). Thus, climate change not only changes the magnitude of energy consumed by EVs over a year, but also changes the timing of the energy use.

Figure 1.35 shows that annual change in EV energy use initially decreases compared to 2018 value reaching a minimum in 2020. After 2020, EV energy use increases again until 2030 and after 2035 the trends in EV energy use for RCP 4.5 and RCP 8.5 diverge. RCP 4.5 shows a reduction in EV energy use while RCP 8.5 shows an increase. This upward and downward swings in energy use are due to the constructive and destructive interaction effects of change in heating/cooling needs and change in efficiency due to ambient temperatures.

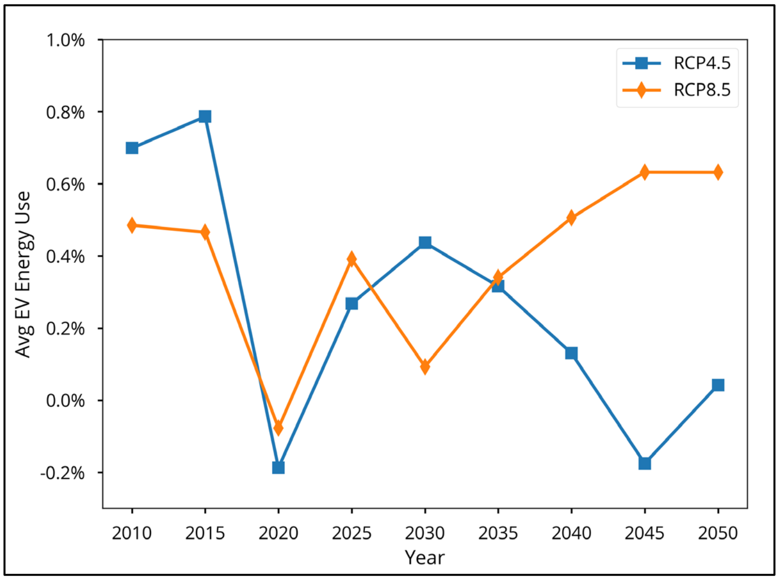

Figure 1.35: Change in EV energy use in the RCP 4.5 and RCP 8.5 scenarios compared with 2018.

To understand what is driving the increase and decrease in EV energy use better, the change in EV energy use for every hour in the year (averaged over the CONUS) is plotted from 2010 to 2050 in Figure 1.36. It is observed that the initial reduction in energy use seen from 2010 to 2020 is mainly due to the milder winters reducing energy use for cabin heating as well as improved efficiency due to better battery performance in the milder weather. However, after 2020, the increased cooling load in summer as well as efficiency dropping due to higher temperatures, negates the energy savings in the winter and net energy use increases again.

The diverging trends in RCP 4.5 and RCP 8.5 observed after 2035 are also evident in Figure 1.36. As discussed before, the RCP 4.5 scenario predicts milder winters and less hot summers compared to RCP 8.5 scenario. As a result, in the RCP 4.5 scenario the energy savings in winter catch back up to increased energy use in summer and net energy use drops. However, in RCP 8.5 scenario, while there is a decrease in winter energy use, the summer energy use increases substantially due to the much warmer temperatures leading to higher overall energy use by 2050.

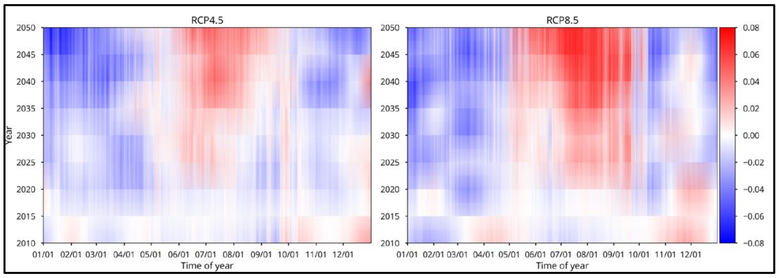

Figure 1.36: Change in average EV energy use over a year from 2010 to 2050 in the RCP 4.5 (left) and RCP 8.5 (right) scenarios.

It is also observed from Figure 1.36 that while the total energy change in Figure 1.35 are small, there is substantial changes in energy use observed at the hourly level. These changes are further magnified at the state level spatial resolution and hourly time resolution. Changes to EV energy use due to climate show expected patterns over the CONUS as seen in Figure 1.37. The warmer states in the southeast see an increase in EV energy use for both the RCP 4.5 and RCP 8.5 scenarios. In the northeast, there are interesting differences in the change to EV energy use in the two climate scenarios. It can be seen that in the RCP 4.5 scenario there is a small increase to EV energy use in the northwestern states, while in the RCP 8.5 scenarios, those states show a reduction in EV energy use. The reason for this is the milder spring weather forecasted in RCP 8.5 scenario, which not only reduces energy use for heating/cooling, but also increase battery efficiency resulting in energy savings.

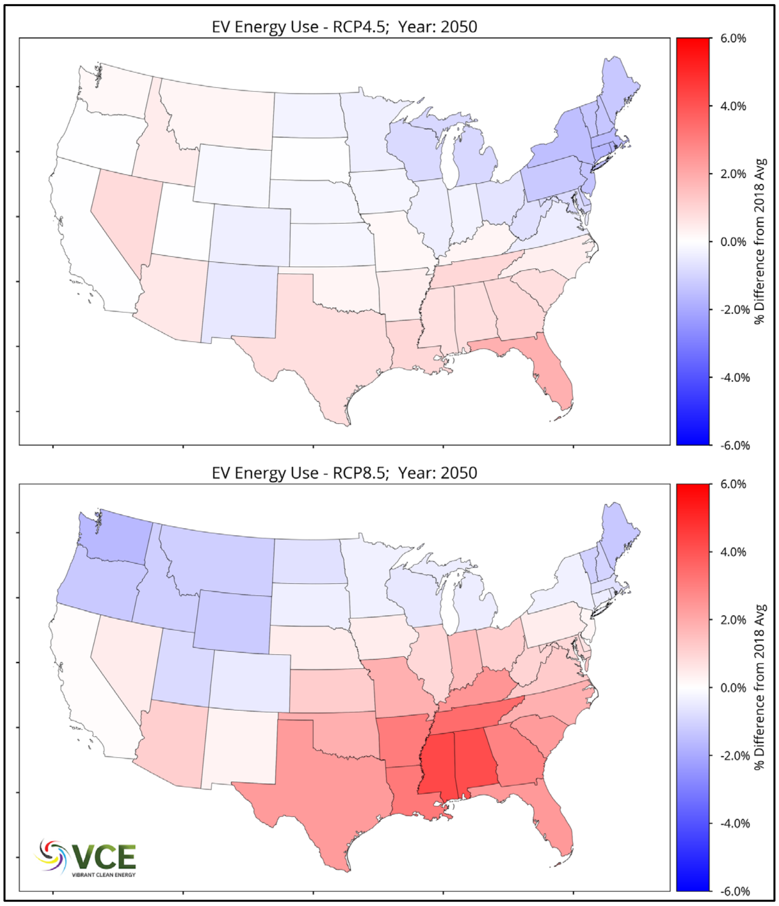

Figure 1.37: Change in EV energy use over the CONUS for the RCP 4.5 scenario (top) and the RCP 8.5 scenario (bottom).

1.6 Bibliography

[1] E. P. James, S. G. Benjamin, and M. Marquis, "A unified high-resolution wind and solar dataset from a rapidly updating numerical weather prediction model," *Renew. Energy*, vol. 102, pp. 390–405, 2017.

[2] J. Wilczak *et al.*, "The wind forecast improvement project (WFIP): A public-private partnership addressing wind energy forecast needs," *Bull. Am. Meteorol. Soc.*, vol. 96, no. 10, pp. 1699–1718, 2015.

[3] J. M. Wilczak *et al.*, "The second wind forecast improvement project (wfip2) observational field campaign," *Bull. Am. Meteorol. Soc.*, vol. 100, no. 9, 2019.

[4] C. T. M. Clack, A. Alexander, A. Choukulkar, and A. E. MacDonald, "Demonstrating the effect of vertical and directional shear for resource mapping of wind power," *Wind Energy*, vol. 19, no. 9, 2016.

[5] A. Choukulkar *et al.*, "A new formulation for rotor equivalent wind speed for wind resource assessment and wind power forecasting," *Wind Energy*, vol. 19, no. 8, 2016.

[6] S. Wharton and J. K. Lundquist, "Atmospheric stability affects wind turbine power collection," *Environ. Res. Lett.*, vol. 7, no. 1, 2012.

[7] A. Betz, "Das Maximum der theoretisch möglichen Ausnutzung des Windes durch Windmotoren," *Gesamte Turbinenwes.*, vol. 17, pp. 307–309, 1920.

[8] C. T. M. Clack, "Modeling solar irradiance and solar PV power output to create a resource assessment using linear multiple multivariate regression," *J. Appl. Meteorol. Climatol.*, vol. 56, no. 1, pp. 109–125, 2017.

[9] J. W. Spencer, "Fourier series representation of the position of the sun," 1971.

[10] D. L. King, J. a Kratochvil, and W. E. Boyson, "Photovoltaic array performance model," *Online*, vol. 8, no. December, pp. 1–19, 2004.

[11] W. De Soto, S. A. Klein, and W. A. Beckman, "Improvement and validation of a model for photovoltaic array performance," *Sol. Energy*, vol. 80, no. 1, pp. 78–88, 2006.

[12] P. Gilman, "SAM Photovoltaic Model Technical Reference SAM Photovoltaic Model Technical Reference," *Sol. Energy*, vol. 63, no. May, pp. 323–333, 2015.

[13] Federal Energy Regulatory Commission, "Form No. 714 - Annual Electric Balancing Authority Area and Planning Area Report," Washington, DC, 2019.

[14] US Energy Information Administration, "U.S. electric system is made up of interconnections and balancing authorities," *Today in Energy*, 2016. .

VCE

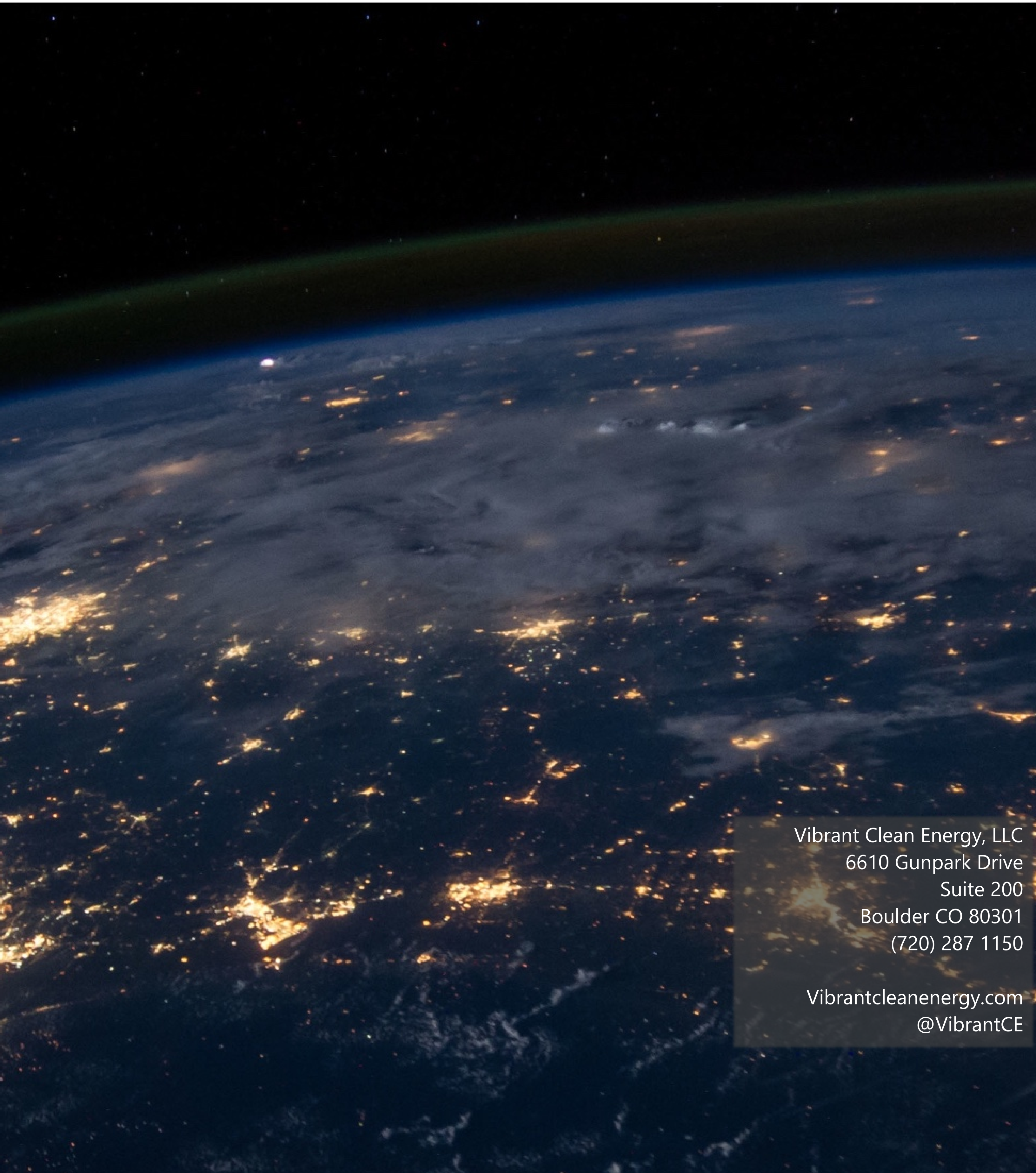

Vibrant Clean Energy, LLC
6610 Gunpark Drive
Suite 200
Boulder CO 80301
(720) 287 1150

Vibrantcleanenergy.com
@VibrantCE